Structure and activation of the human autophagy-initiating ULK1C:PI3KC3-C1 supercomplex

Minghao Chen[1,2,3], Xuefeng Ren[1,2,3], Thanh N. Nguyen[3,4,5,6], Grace Khuu[3,4,5,6], Annan S. I. Cook[2,3,8], Michael Lazarou[3,4,5,6] and James H. Hurley[1,2,3,8,9]*

1. Department of Molecular and Cell Biology, University of California, Berkeley, Berkeley, CA 94720, USA.

2. California Institute for Quantitative Biosciences, University of California, Berkeley, Berkeley, CA 94720, USA.

3. Aligning Science Across Parkinson's (ASAP) Collaborative Research Network, Chevy Chase, MD 20815, USA.

4. Walter and Eliza Hall Institute of Medical Research, Parkville, Victoria, Australia

5. Department of Medical Biology, University of Melbourne, Melbourne, Victoria, Australia

6. Department of Biochemistry and Molecular Biology, Biomedicine Discovery Institute, Monash University, Melbourne, Australia

8. Graduate Group in Biophysics, University of California, Berkeley, Berkeley, CA 94720, USA.

9. Helen Wills Neuroscience Institute, University of California, Berkeley, Berkeley, CA 94720, USA.

* To whom correspondence should be addressed. E-mail: jimhurley@berkeley.edu

Abstract

The unc-51-like kinase protein kinase complex (ULK1C) and the class III phosphatidylinositol (PI) 3-kinase complex I (PI3KC3-C1) are the most upstream and central players in the initiation of macroautophagy in mammals. We found a direct physical interaction between the two complexes. The cryo-EM structures of the human ULK1C core and PI3KC3-C1 were determined at amino acid residue-level resolution, and used to interpret a moderate resolution structure of the ULK1C:PI3KC3-C1 supercomplex. The two complexes co-assemble through extensive contacts between the FIP200 scaffold subunit of ULK1C and the VPS15 pseudokinase subunit of PI3KC3-C1. The presence of PI3KC3-C1 induces a rearrangement of ULK1C from a FIP200:ATG13:ULK1 2:1:1 to a 2:2:2 stoichiometry by dislocating part of the ATG13 intrinsically disordered region ($ATG13^{IDR}$) from an inhibitory site on the dimeric FIP200 scaffold. This suggests a structural mechanism for the initiation of autophagy through PI3KC3-C1-induced dimerization of ULK1 as bound to FIP200, followed by an activating trans-autophosphorylation of ULK1.

Main

Macroautophagy (hereafter, "autophagy") is the main cellular mechanism for the disposal of molecular aggregates and damaged or unneeded organelles[1]. While autophagy was first characterized as a bulk response to starvation, it is now clear that many forms of bulk and selective autophagy are central in development and cellular homeostasis[1]. The homeostatic necessity of autophagy is clearest in neurons, which are post-mitotic and so uniquely susceptible to toxic aggregates and damaged organelles[2]. Autophagic dysfunction has been linked to all major neurodegenerative diseases[2], with the clearest genetic linkage to Parkinson's disease[3].

All forms of canonical autophagy, bulk and selective, are initiated upon the recruitment and activation of the FIP200 protein[4-6] and the class III phosphatidylinositol 3-kinase complex I (PI3KC3-C1)[7-9]. FIP200 is the central scaffolding subunit of the ULK1 complex (ULK1C), which also contains the ULK1 (or ULK2) kinase itself, ATG13, and ATG101[10-14]. PI3KC3-C1 contains one copy each of the lipid kinase VPS34, the pseudokinase VPS15, and the regulatory subunits BECN1 and ATG14[7,15]. The former three subunits are also present in the PI3K complex II (PI3KC3-C2) involved in endosomal sorting and late steps in autophagy, while ATG14 is uniquely involved in autophagy initiation[7]. Atomic and near-atomic resolution structures are known for various fragments of these complexes[16,17], and low to moderate resolution structures are known for human PI3KC3-C1[18,19] and the core of human ULK1C [20].

The means by which ULK1C and PI3KC3-C1 activities are switched on and off are critically important for the physiology of autophagy initiation and for therapeutic interventions targeting neurodegeneration [21]. Yet these mechanisms have thus far been hidden because of the limitations of the available fragmentary or low resolution structures. While ULK1C and PI3KC3-C1 are both critical for autophagy initiation and are both recruited at the earliest stages, beyond the presence of ULK1 phosphorylation sites on PI3KC3-C1 subunits[22,23 ,24,25], it has been unclear how their activities are coordinated. Here we report the structures of the human ULK1C core and PI3KC3-C1 at resolutions adequate for amino acid residue-level interpretation. We also show that ULK1C and PI3KC3-C1 form a physical supercomplex, determine its structure, and show how PI3KC3-C1 regulates the stoichiometry and, potentially, the activity of ULK1C.

Cryo-EM structure of a 2:1:1 stoichiometric ULK1C core

The ordered core of ULK1C was purified in a form consisting of the FIP200 N-terminal domain (1-640) and the ULK1 C-terminal microtubule-interacting and transport (MIT) domain (836-1059) fused with the ATG13 residues (363-517) responsible for binding to FIP200 and ULK1 [20] (Fig 1a). A monodisperse

peak from size exchange chromatography (SEC) was collected and used for cryo-EM data collection. Image processing and 3D reconstruction resulted in a cryo-EM density map with a local resolution of 3.35 Å in the best regions, including the FIP200:ATG13:ULK1 interface (Fig. 1a-g). The distal tips of the FIP200^{NTD} molecules are mobile and the density there is less defined. The ATG13:ULK1 unit resembles the yeast Atg13^{MIM}:Atg1^{MIT} complex [26], so we adopted the MIT/MIM terminology for the human complex. The quality of the density allowed assignment of amino acid residues of the ULK1^{MIT} domain and ATG13^{MIM} (Fig. 1h-l). The structure confirmed the previous observation of a 2:1:1 FIP200:ATG13:ULK1 complex [20], while defining in residue-level detail how ULK1^{MIT} and ATG13^{MIM} bind to FIP200.

The ULK1C core has dimensions of 180 × 130 × 90 Å, contains two molecules of FIP200^{NTD} and one molecule each of ULK1 and ATG13 (Fig. 1b,c). FIP200 ^{NTD} forms a C-shaped dimer as seen at low resolution [20], which can now be described in detail with sequence assigned. The two arms of FIP200 consist of 120 Å-long bundles formed by three twisted helixes (81-495). The two arms are connected by an 80 Å-long dimerization domain (496-599) bent at nearly 90º to the arms, resulting in the C-shape. The structure after residue 599 was not resolved due to presumed disorder. The FIP200 dimer is in some ways reminiscent of the structure of its yeast counterpart, Atg17 [27], although the protein folds are distinct. Atg17 also dimerizes via two arms that are in the same plane, although the arms are arranged in an S-shape instead of a C (Extended Data Fig. 2a). Residues 1-80 of FIP200 form a ubiquitin-like domain (ULD) located at the middle of the Arm domain in the inner side of the C-shape. The higher resolution analysis here confirms the previous observation that the ULD and the Arm domain of FIP200 have the same fold as the scaffold domain of the Tank-binding kinase 1 (TBK1) [20] (Extended Data Fig. 2b), which is itself central to the initiation of some forms of autophagy [28].

Cryo-EM density of for one copy of a ULK1^{MIT}:ATG13^{MIM} heterodimer was observed on one "shoulder" of the FIP200 dimer. The ATG13^{MIM} binds collaboratively to both FIP200 and ULK1^{MIT} (Fig. 1d, Extended Data Fig. 2c), consistent with the role of ATG13 in recruiting ULK1[29] downstream of FIP200. As seen for yeast Atg13:Atg1[26], the structure consists of two four-helix bundles. Three helices of each are from the ULK1^{MIT} and one from the ATG13^{MIM}. Four pairs of hydrophobic residues from the ATG13^{MIM} form prominent direct interactions with ULK1^{MIT} (Extended Data Fig. 2c). The ULK1^{MIT}:ATG13^{MIM} heterodimer binds to FIP200 via two main interfaces (Extended Data Fig. 2d-g). Three FIP200 residues, Val314, Arg326, and Arg334, were identified as important for the ATG13 interaction on the basis of mutagenesis and Strep pull-down assays (Extended Data Fig. 2h).

The ATG13^{IDR}:FIP200^{NTD} interface

The C-terminal portion of the ATG13 intrinsically disordered region (ATG13$^{IDR)}$, corresponding to residues 363-460, was previously demonstrated to bind to the FIP200^{NTD} [20], but was not visualized with sufficient continuity to assign amino acid sequence on the basis of the density alone. In this study, we utilized AlphaFold2[30] as corroborated by HDX-MS [20] to map four potential binding sites on ATG13 (#1(370-387), #2(392-408), #3(409-414)), and #4(450-460)) (Fig 2a,b). The interaction of a single ATG13^{IDR} extends through both protomers of the FIP200^{NTD} dimer. Sites #1 and #4 are unique in ATG13, but their binding sites on two FIP200 protomers are structurally symmetric. One FIP200 molecule is occupied by ATG13 site #4 and the ULK1^{MIT}:ATG13^{MIM} heterodimer, and the other FIP200 molecule is occupied by site #1-3 of the ATG13^{IDR} loop. This explains the unusual 2:1:1 stoichiometry of the ULK1C by showing why the FIP200^{NTD} dimer only binds one copy of ATG13 in the complex.

We screened a series of truncations to map the FIP200 binding determinants of ATG13^{IDR}. Two ATG13 fragments, 363-398 (corresponding to site #2), and 450-460 (site #4) were independently sufficient for the FIP200 binding, consistent with previous HDX-MS data[20]. Point mutagenesis showed that ATG13 residues Phe394, Phe397, and Glu403, and FIP200 residues Leu324, Arg543, and Arg548, are key to binding site #2 (Fig 2c-e), and ATG13 residues Ala452 and Phe453, and FIP200 Val44 are key for the binding site #4 (Fig 2f, g). We tested disrupting the binding between ATG13 and FIP200 would affect PINK1/Parkin-dependent mitophagy in response to Oligomycin and Antimycin A (OA) treatment. FIP200 variants were introduced into *FIP200* KO HeLa cells expressing Parkin, and mitophagy rescue was assessed by using a Halo-based assay. We expected binding of ATG13 to sites 2 could compensate for loss of binding to 4, and vice versa. We therefore tested the function of both single and multisite FIP200 mutations. The first steps in PINK1/Parkin mitophagy can bypass ULK1 recruitment via the OPTN-TBK1-PI3KC3-C1 axis, while NDP52 can utilize either ULK1 or TBK1, [31] and therefore a full loss of function was not expected. Most FIP200 mutations did not lead to an evident loss of function. The multisite FIP200 mutant V44D/V314D/L324D/R543D/R548D did lead to a statistically significant decrease in mitophagic flux, supporting that interaction between ATG13^{IDR}:FIP200^{NTD} plays an important role in PINK1/Parkin mitophagy (Fig 2h,i).

Cryo-EM structure of PI3KC3-C1

The structure of the PI3KC3-C1 and the related PI3KC3-C2 complex, involved in late stages in autophagy and in endosomal sorting [15] has been extensively studied [18,19,32-36], yet still no structures of the autophagy-specific PI3KC3-C1 have been resolved at a high enough resolution to place amino acid side chains. Here, we determined the PI3KC3-C1 structure at a best local resolution of 3.26 Å, allowing

accurate model building with side-chain assignment (Fig. 3, Extended Data Fig. 3). The refined structure is in a similar overall conformation to that of the PI3KC3-C1-NRBF2 complex [18] and the density quality facilitated building a high-confidence molecular model (Extended data Fig. 4). The VPS34^{KD} (kinase domain) was not visualized, consistent with past observations of its flexibility [35] (Fig. 3a, Extended data Fig. 3c). The VPS15^{HSD} (helical solenoid domain)-VPS34^{C2} core is the best-resolved region of the complex (Extended data Fig. 3e). The BECN1^{BARA}-ATG14L^{BLD} (BARA-like domain)-VPS15^{WD40} forms a rigid tertiary subcomplex, and its position relative to the VPS15^{HSD}-VPS34^{C2} core is dynamic (Extended data Fig. 3f). A nucleotide diphosphate (NDP) molecule is bound in the VPS15^{PKD} (pseudo-kinase domain) catalytically inactivated cognate of the kinase active site (Extended data Fig. 5a,b). The resolution of the density was insufficient to conclusively identify the nucleotide, but further work identified it as GTP [37]. VPS15^{PKD} contains an Ala at the position where a Gly is required for full kinase catalytic activity, but in most other respects matches the motifs and structure expected for an active protein kinase (Extended data Fig. 5c,d). This reconstruction thus allowed us to accurately assign the amino acid residues to the three-dimensional structure and identify that an NDP is stably bound to VPS15.

ULK1C and PI3KC3-C1 form a supercomplex via FIP200 and VPS15

It has been unclear whether PI3KC3-C1 is recruited coordinately with ULK1C by a direct mutual interaction *versus* some other mechanism. To determine if there was a direct interaction, and if so, with which portion of the complex, we assessed binding of PI3KC3-C1 to the ULK1C core and the ATG13-ATG101 HORMA dimer. Robust direct binding between FIP200 and the PI3KC3-C1 was observed by pull-down and bead binding assays (Fig. 4a). The ATG13-ATG101 HORMA dimer does not strongly interact with PI3KC3-C1 under these conditions (Fig. 4b, c). ULK1C and PI3KC3-C1 were mixed and visualized by cryo-EM (Extended data Fig. 6a). A small population of ULK1C core in complex with PI3KC3-C1 was observed in this dataset (Extended data Fig. 6b). The mixture was then further purified by MBP pull-down FIP200^{NTD}-MBP and the eluate subjected to cryo-EM (Extended data Fig. 7a-f). A larger class of the ULK1C-PI3KC3-C1 supercomplex was obtained, in which both the C-shaped density of the ULK1C core and the V-shaped density of the PI3KC3-C1 are clearly observed (Fig. 4d). Even though the 3D reconstruction was limited to a resolution of 6.3 Å, the map quality was sufficient to dock the higher resolution models of the individual complexes (Fig. 4e).

The main interface of the supercomplex is formed between the globular FIP200^{ULD} domain of the ULK1C and the curved VPS15^{HSD} domain of PI3KC3-C1. The interaction is mediated by three hydrophobic clusters (FIP200$^{A39/I40}$:VPS15^{V566}, FIP200^{L80}:VPS15$^{A606/L645/L647}$,

FIP200$^{F457/L460}$:VPS15^{I686}) (Extended data Fig. 7g,h,k). The same general surface of VPS15^{HSD} binds NRBF2 and UVRAG^{C2} in the PI3KC3-C1 and -C2, respectively[18,33] (Extended data Fig. 7i,j).

Formation of a 2:2:2 ULK1 core complex induced by PI3KC3-C1

In the same ULK1C:PI3KC3-C1 data set described above, a particle class of ULK1C alone showing clear 2:2:2 stoichiometry was obtained (Fig. 5a, Extended data Fig. 6c). The presence of the ULK1^{MIT}-ATG13^{MIM} heterodimer was confirmed on both of the FIP200 shoulders, demonstrating that the stoichiometry of the ULK1 complex is altered by the presence of PI3KC3-C1. The supercomplex structure showed that the N-terminus of the BECN1 and ATG14L binds near ATG13 sites #1-3 on FIP200. The interaction with site #2 is asymmetric and we therefore hypothesized that its main role is to inhibit 2:2:2 ULK1C formation. We hypothesized that PI3KC3-C1 acts by displacing the ATG13 from site #2, and potentially, sites #1 and 3. To test this model, we truncated ATG13^{IDR} at residue 449 and determined the cryo-EM structure of an ATG13$^{450-517}$-containing version of the ULK1C core in the absence of PI3KC3-C1. The 2D averages clearly show densities ULK1^{MIT}-ATG13^{MIM} heterodimer on both sides of the shoulder (Fig. 5b), which was confirmed by 3D reconstruction at 4.46 Å (Extended Data Fig. 2d-h). The stoichiometry was investigated in solution by size-exclusion chromatography with in-line multi-angle light scattering (SEC-MALS). The ULK1C cores in the presence and absence of the ATG13^{IDR} region displayed masses consistent with 2:1:1 and 2:2:2 complexes, respectively, consistent with the cryo-EM data. Furthermore, the ATG13 mutant F394D/F397D/E403K, designed to disrupt site #2, also formed a complex with a 2:2:2 stoichiometry (Fig. 5c). This finding demonstrated that the site #2 of ATG13^{IDR} has an inhibitory function on recruitment of the second ULK1 kinase to the FIP200 dimer, which is relieved upon formation of the supercomplex with PI3KC3-C1.

Discussion

Despite that ULK1C and PI3KC3-C1 are at the heart of human autophagy initiation [38], there have been three major gaps in understanding how autophagy is switched on by these two complexes. First, the available structures have been either too fragmentary or at inadequate resolution to draw mechanistic conclusions about the integrated regulation of the entire complexes. Second, beyond the ability of ULK1 to phosphorylate all four subunits of PI3KC3-C1[22,23,24,25], it has been unclear how the activities of the two complexes are coordinated. Third, thinking about activation of ULK1C, in particular, has been centered on its response to nitrogen starvation and mTORC1 inhibition (mTORCi) [10,11,13]. Yet the physiological pathways of greatest biomedical importance, notably in neurobiology, are largely independent of mTORCi [39].

Here, we filled the first gap with cryo-EM reconstructions of the ULK1C core and PI3KC3-C1 that permit amino acid-level interpretation. Remaining gaps in the structure were filled in by AlphaFold2 predictions validated against pre-existing HDX-MS data and site-directed mutagenesis [20]. With respect to the second gap, we found that ULK1C and PI3KC3-C1 form a physical complex mediated by FIP200 and VPS15 subunits. The ULK1C core, which lacks the ATG13:ATG101 HORMA domains, binds PI3KC3-C1 stably enough to yield a cryo-EM reconstruction. This differs from a recent report that ULK1 binds to a BECN1:ATG14 subcomplex of PI3KC3-C1 only in the presence of an ATG9 complex and only with full-length HORMA domain-containing ATG13 and ATG101 [40]. In contrast, we found that the ATG13:ATG101 HORMA dimer interacts only weakly with the complete PI3KC3-C1 (Fig. 4b), and that the presence of ATG9 is not needed for the two complexes to interact. In yeast, the Atg1 complex (the yeast counterpart of human ULK1C) and PI3KC3-C1 are also reported to be in direct physical contact, which mediates the recruitment of PI3KC3-C1 to the phagophore initiation site in yeast[41]. The determinants of binding appear, however, to differ between yeast and humans. Among other differences, Atg38 is important for PI3KC3-C1 recruitment in yeast[41], while we found that the human supercomplex assembles independently of the human Atg38 ortholog NRBF2. With respect to the third gap, the observation that PI3KC3-C1 binding to ULK1C triggers a rearrangement of ULK1C from a 2:1:1 to a 2:2:2 complex. The rearrangement suggests a mechanism for activation that depends on the co-recruitment of ULK1C and PI3KC3-C1, but does not conceptually depend on any particular upstream pathway.

ULK1 kinase activity requires autophosphorylation at Thr180 [42], as does its yeast ortholog, Atg1 [43]. Artificially induced dimerization of yeast Atg1 is known to promote its activation [44,45]. The dimerization and subsequent autophosphorylation of receptor-linked tyrosine kinases (RTKs) is the central paradigm for kinase activation in growth factor signaling [46]. These findings suggest that PI3KC3-C1- and ATG13-regulated ULK1 kinase dimerization is the autophagic cognate of the dimerization-based RTK activation paradigm (Fig.5c). The presence of an excess of 2:2:2 ULK1C cores relative to ULK1C: PI3KC3-C1 supercomplexes suggests that PI3KC3-C1 acts as an exchange factor to promote the 2:2:2 complex, serving to displace ATG13 from the autoinhibitory site #2. This model suggests that PI3KC3-C1 does not need to remain tightly bound in a supercomplex to ULK1C following activation (Fig.5c), but PI3KC3-C1 would be susceptible to phosphorylation by ULK1[22,23,24,25].

Most, but not all, autophagy initiation pathways require ULK1/2. In OPTN-mediated Parkin-dependent mitophagy, TBK1 replaces the requirement for ULK1/2 [28]. However, ATG13 and FIP200 are still essential for this pathway, as confirmed here by the phenotype observed for ATG13-binding deficient FIP200 mutations. We found that TBK1 contains a scaffold domain that closely resembles the arm of FIP200 involved in binding to VPS15 (Extended Data Fig. 2b and Extended Data Fig. 7h), and TBK1 has been shown to bind directly to PI3KC3-C1[28]. It will be interesting to determine if TBK1 uses its FIP200 arm-like domain to bypass the need for ULK1/2 in OPTN mitophagy. The role of the VPS15 pseudokinase domain in PI3KC3 function has been a mystery since its initial identification in yeast[47]. We recently found that VPS15 is a GTP-binding myristoyl switch that regulates the lipid kinase activity of PI3KC3[37]. Here, we established a role for VPS15 as the major bridge to FIP200 in ULK1C recruitment.

Given the large interface between VPS15 and FIP200, and the multiple contacts between the $ATG13^{IDR}$ and FIP200, various upstream kinases and other signaling inputs could regulate formation of the ULK1C:PI3KC3-C1 supercomplex and the activated 2:2:2 ULK1C. While mTORC1 is one candidate to modulate these complexes, these mechanisms are in principle general and could be regulated by other kinases such as AMPK[48] or TBK1[49], or by colocalization driven by selective autophagy cargo receptor clustering[50] or condensate formation[51]. The new activation-related interfaces identified in this study are, of course, also suggestive of new concepts for the therapeutic upregulation of autophagy. The concept of ULK1C:PI3KC3-C1 supercomplex formation at the heart of autophagy initiation thus puts both the signaling and therapeutic aspects of autophagy initiation into new perspective.

Materials and Methods

Plasmid construction

The sequences of all DNAs encoding components of human ULK1C were codon optimized, synthesized and then subcloned into the pCAG vector. The fusion construct of ATG13 C-terminal with $ULK1^{MIT}$ domain was subcloned as a TwinStrep-Flag (TSF), TEV cleavage site, ATG13 (363-517) or (450-517), 5 amino acid linker (GSDEA) followed by ULK1 (836-1050) into the pCAG vector. Proteins were tagged with GST, MBP or TSF for affinity purification, pull-down or GSH beads assay. All constructs were verified by DNA sequencing. Details are shown in Table 1.

Protein expression and purification

For cryo-EM samples of $FIP200^{NTD}$:$ATG13^{363-517}$-$ULK1^{MIT}$ complexes, pCAG-$FIP200^{NTD}$ (1-640) was co-transfected with pCAG-TSF-$ATG13^{363-517}$-$ULK1^{MIT}$ (836-1050) using the polyethylenimine (PEI) (Polysciences) transfection system. $FIP200^{NTD}$-MBP:$ATG13^{363-517}$-$ULK1^{MIT}$-TSF were co-expressed in HEK293 $GnTi^-$ cells for the FIP200:PI3KC3-C1 cryo-EM study. Cells were transfected at a concentration of 2×10^6/ml. After 48 hours, cells were pelleted at 500x g for 10 min, washed with PBS once, and then stored at −80°C. Cell pellets were lysed at room temperature for 20 min with lysis buffer (25 mM HEPES pH 7.5, 200 mM NaCl, 2 mM $MgCl_2$, 1 mM TCEP, 10% Glycerol) with 5 mM EDTA, 1% Triton X-100 and protease inhibitor cocktail (Thermo Scientific) before being cleared at 17000x rpm for 35 min at 4 °C. The clarified supernatant was purified on Strep-Tactin Sepharose resin (IBA Lifesciences) and then eluted in the lysis buffer with 4mM desthiobiotin (Sigma). After His_6-TEV cleavage at 4°C overnight, samples were concentrated then load onto a Superose 6 Increase 10/300 GL column (Cytiva) in the buffer of 25 mM HEPES pH 7.5, 150 mM NaCl, 1 mM $MgCl_2$, 1 mM TCEP.

PI3KC3-C1 complex was expressed in HEK293 $GnTi^-$ cells via PEI transfection from codon optimized pCAG-VPS15-TSF, pCAG-VPS34, pCAG-ATG14 and pCAG-Beclin-1. pCAG-GST-ATG14 or pCAG-mCherry-ATG14 was used in PI3KC3-C1 expression for GST pull-down or microscopy-based GSH bead assay. Cells were transfected at a concentration of 2×10^6/ml and harvested after 48 hour post-transfection. Pellets were homogenized 20 times by Pyrex douncer (Corning) in lysis buffer with 25mM TCEP/proteinase inhibitors (Thermo Scientific), and then add 10% Triton X-100 stock to final 1% concentration. After rocking at 4 °C for 1 hour, lysates were clarified by centrifugation (17,000 x rpm for 40 min at 4 °C) and incubated with Strep-Tactin Sepharose (IBA Lifesciences) at 4 °C overnight. After eluting with lysis buffer/4 mM desthiobiotin, samples were concentrated and then loaded onto a Superose

6 Increase 10/300 GL column (Cytiva) in 25 mM HEPES pH 7.5, 300 mM NaCl, 1 mM $MgCl_2$, 25 mM TCEP. $FIP200^{NTD}$ constructs used in Figure 4b, c were purified using strep-tactin Sepharose resin as described above, and then loaded onto a Superose 6 Increase 10/300 GL column (Cytiva). ATG101:ATG13N HORMA related proteins in Figure 4b, c were purified using strep resin and a Superdex 200 Increase 10/300 GL column (Cytiva) equilibrated in 25 mM HEPES pH 7.5, 150 mM NaCl, 1 mM $MgCl_2$, 1 mM TCEP.

Strep pull-down assay

$FIP200^{NTD}$-TSF WT or mutants were co-transfected with GST-$ATG13^{363-517}$ and/or $ULK1^{MIT}$-MBP in 10 ml of HEK293 $GnTi^-$ cells. The cells were harvested 48 hours after transfection. The pellets were homogenized in 0.5 ml of lysis buffer/protease inhibitors/1% TritonX-100, and clarified after 40,000g x 15 min. The lysate was incubated with 30 µl Strep-Tactin Sepharose resin (IBA-Lifesciences) at 4°C for 3 hours. The beads were washed four times, and then eluted in 50 µl lysis buffer/4 mM desthiobiotin. 18 µl eluent was mixed with lithium dodecylsulfate (LDS)/BME buffer, heated at 60°C for 5 min and subjected to SDS/PAGE gel. The gel was then stained with Coomassie brilliant blue G250.

GST pull-down assay

GST tagged protein and fluorescent protein were mixed with 30 µl Glutathione Sepharose beads (Cytiva) at final 1 µM concentration in the buffer of 25 mM HEPES at pH 7.5, 150 mM NaCl, 1 mM $MgCl_2$ and 1 mM TCEP. The total volume is 200 µl. After rocking at 4°C overnight, the beads were washed four times, then eluted in 50 µl of buffer/25 mM glutathione. 18 µl eluent was mixed LDS/BME buffer and subjected to SDS/PAGE gel without heating samples. The gel was scanned at 488 or 550 nm in ChemiDoc MP imaging system (Bio-Rad).

Microscopy-based GSH bead protein-protein interaction assay

A mixture of 1 µM purified GST tagged protein and 500 nM purified fluorescent protein in total 70 µl volume was incubated with 9 µL pre-blocked Glutathione Sepharose beads (Cytiva) in a reaction buffer containing 25 mM HEPES at pH 7.5, 150 mM NaCl, 1 mM $MgCl_2$ and 1 mM TCEP. After incubation at room temperature for 30 min, samples were mixed with additional 100 µL reaction buffer, and then transferred to the observation chamber for imaging. Images were acquired on a Nikon A1 confocal microscope with a Nikon Plan APO VC 20x/0.75 NA UV Microscope Objective. Three biological replicates were performed for each experimental condition.

Size Exclusion Chromatography with Multiangle Light Scattering (SEC-MALS)

The purified FIP200^{NTD}:ATG13-ULK1^{MIT} complexes were concentrated to 4-5 mg/ml. SEC-MALS experiments were performed using an Agilent 1200 HPLC system (Agilent Technologies, Santa Clara, CA), coupled to a Wyatt DAWN HELEOS-II MALS instrument and a Wyatt Optilab rEX differential refractometer (Wyatt, Santa Barbara, CA). For chromatographic separation, a WTC-050S5 size-exclusion column (Wyatt) with a 40 µl sample loop was used at a flow rate of 0.3 ml/min in the buffer of 25 mM HEPES pH 7.5, 200 mM NaCl, 1 mM $MgCl_2$, 2 mM TCEP. The outputs were analyzed by the ASTRA V software (Wyatt). MALS signals, combined with the protein concentration determined by refractive index, were used to calculate the molecular mass of the complex.

Sample preparation of FIP200:PI3KC3-C1 complex for cryo-EM

FIP200^{NTD}-MBP:ATG13$^{363-517}$-ULK1^{MIT}-TSF (final 5 µM) was mixed with PI3KC3-C1-TSF complex at 1:1.5 molar ratio in total 200 µl volume, rocking at 4°C overnight. Next day, the sample was incubated with 50 µl amylose resin (New England Biolab) at 4°C for 3 hr. After one wash, the beads were eluted in 50 µl of 35 mM Maltose with the buffer of 25 mM HEPES pH 7.5, 200 mM NaCl, 1 mM $MgCl_2$, 25 mM TCEP.

Cloning and generation of stable cell lines

mCherry-tagged FIP200 wild type (WT) and mutants (V44D; V314D; V44D/V314D; L324D/R543/R548D; V44D/V314D/L324/R543/R548D were subcloned into pCDH1-CMV-MCS-SV40-hygromycin lentiviral vector using NheI and BamHI restriction enzyme sites. Generation of stable cell lines were previously described [31,52] and available at protocols.io (doi.org/10.17504/protocols.io.dm6gpjzm8gzp/v1). BFP-Parkin (Addgene, 186221) and pSu9-Halo-GFP (Addgene, 184905) were stably expressed in *FIP200* KO cells using lentiviral transduction. Cells positive for both BFP and GFP were then sorted by flow cytometry. mCherry-tagged FIP200 variants were stably introduced into *FIP200* KO cells expressing BFP-Parkin and pSu9-Halo-GFP via lentiviral transduction. Equal expression levels of different FIP200 variants were achieved via FACS sorting for equal mCherry signal.

Halo assay to assess mitophagy

A Halo-based assay to measure mitophagy was recently developed using pSu9-Halo-mGFPplasmid (Addgene, 184905) [53]. The protocol is available at dx.doi.org/10.17504/protocols.io.dm6gpjzm8gzp/v1. Mitophagy induction was carried out as described in refs.[31,54]. Briefly, 350,000 cells were seeded the day

before the mitophagy induction in 6 well plates. The cells were then treated with 50 nM TMR-conjugated Halo ligand in growth media growth media (DMEM with 10% FBS, 4.5 g/l Glucose (Sigma, G8769), 1x GlutaMAX™ (ThermoFisher, 35050061), 1x MEM NEAA (ThermoFisher, 11140-050), 25 mM HEPES (1688449)). After 15 min incubation, the cells were then washed twice with 1x PBS and treated with growth media containing 4 μM Antimycin A (Sigma, A8674), 10 μM Oligomycin (Calbiochem, 495455) and 10 μM QVD (MedChemExpress, HY-12305) for the indicated time periods. Following treatment, the cells were washed with ice-cold 1x PBS, harvested using cell scrapers and lysed in lysis buffer (1× LDS sample buffer (Life Technologies) containing 100 mM dithiothreitol (DTT; Sigma)). Samples were boiled at 99 °C with shaking for 7 min and 25 μg of protein per sample was analysed with 4-12% Bis-Tris gels (Life Technologies) according to manufacturer's instructions. Gels were electro-transferred to polyvinyl difluoride membranes (PVDF) and immunoblotted with antibodies against VCP (Cell Signaling, 2649), HALO (Promega, G9211). For quantification, band intensities were measured using ImageLab 5.2.1 (BioRad). Statistical significance was calculated from four independent experiments using two-way ANOVA. Error bars are means ± standard deviation.

Sample vitrification and cryo-EM data acquisition

For cryo-EM sample preparation, 3 μl of protein solution was applied onto a grid freshly glow-discharged in PELCO easiGlow system (Ted Pella). In-house graphene grids were prepared from Trivial Transfer Graphene sheets (ACS Material) and QUANTIFOIL R2/1 mesh 300 gold (Electron Microscopy Sciences) by following a protocol introduced by Ahn et., al [55]. The graphene grids were used for the ULK1C (2:1:1) core sample, and holey carbon grids (QUANTIFOIL R1.2/1.3 or R2/1 mesh 300, Electron Microscopy Sciences) were sufficient for the other samples. The samples were vitrified with a Vitrobot cryo-plunger (Thermo Fisher Scientific) in plunging conditions optimized previously. The final concentration of each sample was summarized in Table 1. 0.05%(w/v) of n-Octyl-Beta-D-Glucopyranoside was added in the sample solution as a surfactant before vitrification.

The datasets of ULK1C (2:1:1) core and the ULK1C:PI3KC3-C1 mixture were recorded at a 300 kV Titan Krios microscope (Thermo Fisher Scientific) equipped with X-FEG and energy filter set to a width of 20 eV. Automated data acquisition was achieved using SerialEM [56] on a K3 Summit direct detection camera (Gatan) at a magnification of 81,000x and a corresponding pixel size of 1.05 Å and a defocus range of -0.8 to -2.0 μm. Image stacks with 50 frames was collected with a total dose of 50 e/Å^2. The other three datasets (i.e. the ULK1C (2:2:2) core, PI3KC3-C1, and the ULK1C:PI3KC3-C1 pull-down) were recorded at a 200 kV Talos Arctica microscope (Thermo Fisher Scientific) equipped with

the K3 Summit camera in a super-resolution correlated-double sampling mode. The magnification and the pixel size were 36,000x and 0.5575 Å at the super-resolution mode, respectively. Other details of the dataset collection are summarized in Table 2.

Image processing and 3D reconstruction

The datasets were processed by following the workflow in cryoSPARC v4.1.1 [57]. In brief, the super-resolution video stacks were motion-corrected and binned 2x by Fourier cropping using Patch Motion Correction. Contrast transfer function determination was done by Patch CTF Estimation, followed by manual removal of the outlier micrographs base on the estimated defocus and resolution value. Single particles were automatically picked by Topaz [58] based on a manually trained model and extracted with a window size that is 1.5 times larger than the target particle and further binned to 2-4x to facilitate the following processing. Two-dimensional (2D) classification was then used for removing obvious junk particles for the following classification. The initial models were obtained by using *ab initio* reconstruction. In case the reconstruction job failed to give a healthy initial model, the classes displaying high-resolution features in the 2D classification step were selected and used for *ab initio* reconstruction. Further classification was done at the 3D level by multiple rounds of heterogeneous refinement until a clean substack was obtained. The particles were re-extracted with the refined coordinates on micrographs at the original bin 2x pixel size and used for homogeneous refinement for multiple rounds until the final resolution converges. To further improve the quality of the map, local refinement was applied to the datasets of the ULK1C (2:1:1) core and the PI3KC3-C1. Masking areas were decided by 3D Variability or 3D Flex and the masks were created by UCSF ChimeraX v1.5 [59] and Volume Tools. Each local map was aligned to the consensus map and composed by using EMAN2 [60]. The composed maps were then used for model building. The details of data processing are summarized in Table 2.

Model building, validation, and visualization

The *in silico* models of the ULK1C (2:1:1) core and the full length PI3KC3-C1 were generated by AlphaFold2 prediction [30]. The resolution of the observed maps enabled amino acid sequence assignment. The primary and secondary structure of the predicted models agrees well with the EM maps. A flexible model fitting by using the real-time molecular dynamics simulation-based program ISOLDE [61] implemented in the visualization software UCSF ChimeraX was performed, followed by iteratively refinement by using the model editing software Coot [62] manually and real-space refinement in Phenix [63] automatically.

The 3.26 Å resolution map of PI3KC3-C1 clearly showed side chain features and enabled us to assign a revised sequence register for VPS15^{HSD} (Extended data Fig. 4a) relative to the homology-based prediction of the only previous related structure with an original sequence assignment [33]. Based on the present map, the residues 527-545 and 550-568 are assigned to the 9th and 10th helixes of the VPS15^{HSD}, respectively. This assignment is consistent with the Alphafold2 prediction (Extended data Fig. 4b).

The two ULK1C (2:2:2) core models were created by aligning two copies of FIP200^{NTD}: ATG13$^{363-517}$:ULK1^{MIT} sub-trimeric complex to the FIP200 dimerization domain, followed by flexible model fitting with using ISOLDE in ChimeraX. The side chains were removed because of the moderate resolution of these maps. The ULK1C:PI3KC3-C1 supercomplex coordinates were generated by rigid fitting of the individual structures of the ULK1C (2:1:1) and the PI3KC3-C1 to the cryo-EM map. The side chains were removed. The quality of the models was validated by using the validation tools in Phenix and the online validation service provided by wwPDB [64,65]. The details of the model quality assessment are summarized in Table 2. All the figures and videos were made using UCSF ChimeraX.

Acknowledgments

We thank A. Yokom and X. Shi for contributing to early stages of the project, and all members of the Hurley Lab, and D. Fracchiolla and others in Aligning Science Across Parkinson's (ASAP) Team mito911 for advice and discussions. We thank D. Toso, P. Tobias and R. Thakkar for cryo-EM facility support.

Funding

This research was funded by Aligning Science Across Parkinson's [ASAP-000350] through the Michael J. Fox Foundation for Parkinson's Research (MJFF) (M.L. and J.H.H.).

Data availability

The cryo-EM maps were deposited in the Electron Microscopy Data Bank (EMDB) under accession codes EMD-40658 (ULK1C (2:1:1) core), EMD-40669 (PI3KC3-C1), EMD-40738 (ULK1C:PI3KC3-C1 supercomplex), EMD-40715 (ULK1C (2:2:2) core in the PI3KC3-C1 mixture), and EMD-40735 (ULK1C (2:2:2) core of the ATG13$^{450–517}$ truncation mutant). The structural coordinates were deposited in the Protein Data Bank (PDB) under accession codes 8SOI (ULK1C (2:1:1) core), 8SOR (PI3KC3-C1), 8SRQ (ULK1C:PI3KC3-C1 supercomplex), 8SQZ (ULK1C (2:2:2) core in the PI3KC3-C1 mixture), and 8SRM (ULK1C (2:2:2) core of the ATG13$^{450–517}$ truncation mutant). Protocols were deposited in protocols.io. Plasmids developed for this study were deposited at Addgene.org. Raw data files for gel scans were uploaded to Zenodo.

Author contributions

Conceptualization: J.H.H. Methodology: M.C., X.R., T.N.N., G.K. and A.C. Investigation: M.C., X.R., T.N.N. and A.C. Visualization: M.C. Supervision: M.L. and J.H.H. Writing—original draft: M.C. and J.H.H. Writing—review and editing: All authors.

Competing interests

J.H.H. is a cofounder of Casma Therapeutics and receives research funding from Genentech and Hoffmann-La Roche. M.L. is a co-founder and member of the scientific advisory board of Automera. The other authors declare that they have no competing interests.

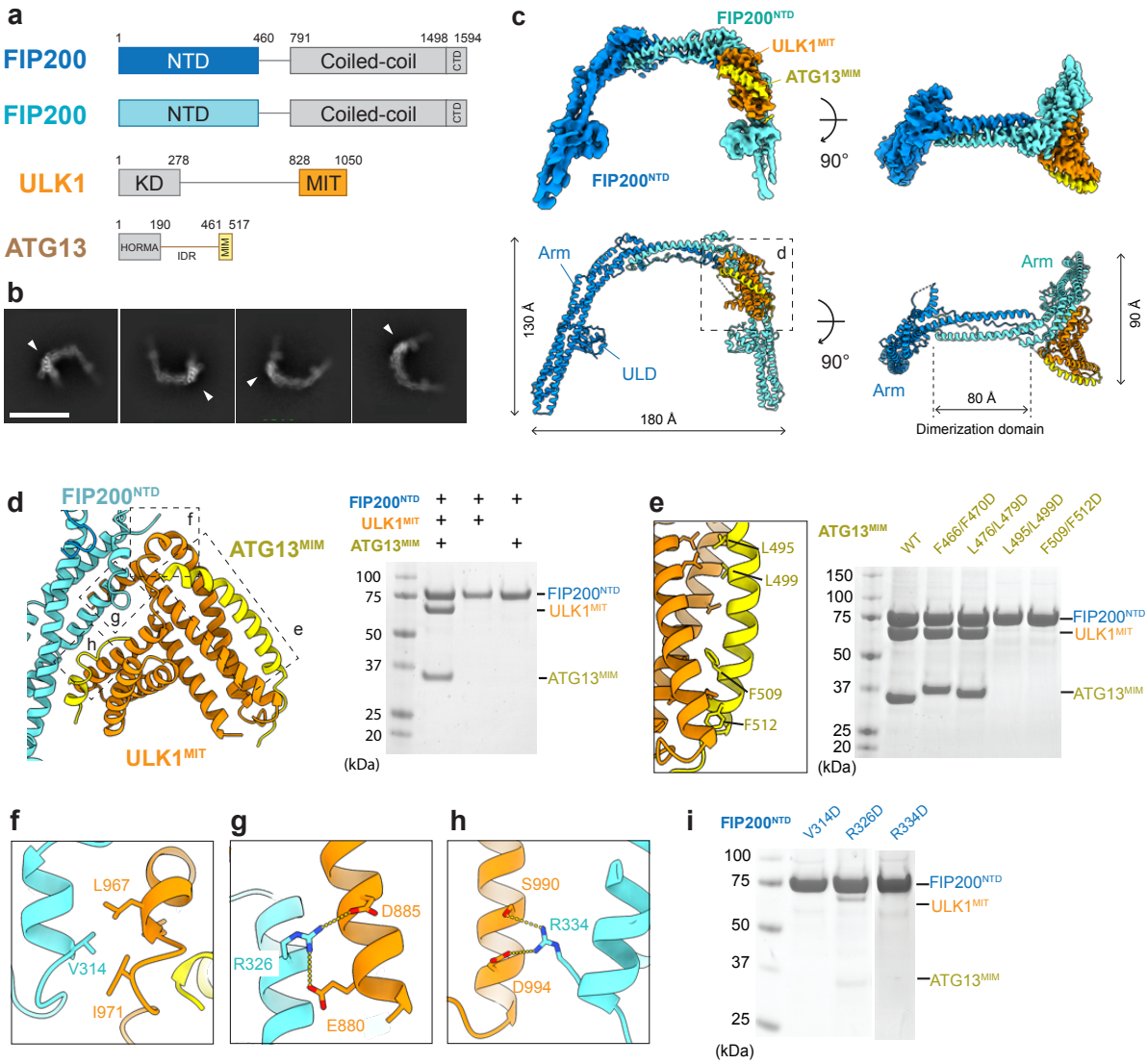

Fig. 1 Structure of the ULK1C core.

a. Domain organization of the ULK1C core. Gray indicates the regions truncated in this study. NTD: N-terminal domain, CTD: C-terminal domain, KD: Kinase domain, MIT: Microtubule-interacting and transport domain, HORMA: Hop1p/Rev7p/MAD2 domain, MIM: MIT-interacting motif. **b**. Representative reference-free 2D class averages of the ULK1C core. Scale bar: 20 nm. **c**. Overview of the EM map (upper) and the coordinates (lower) of the ULK1C core. Subunits are depicted in the same color as in (**a**). The map is contoured at 12σ. **d**. Cooperative binding of FIP200^{NTD} to ULK1^{MIT} and ATG13^{MIM}. **e**. Close-up view of the interface between ULK1^{MIT} and ATG13^{MIM} and the corresponding Strep pulldown assay. **f-i**. Close-up view of the interface between ULK1^{MIT} and FIP200 and the corresponding Strep pulldown assay.

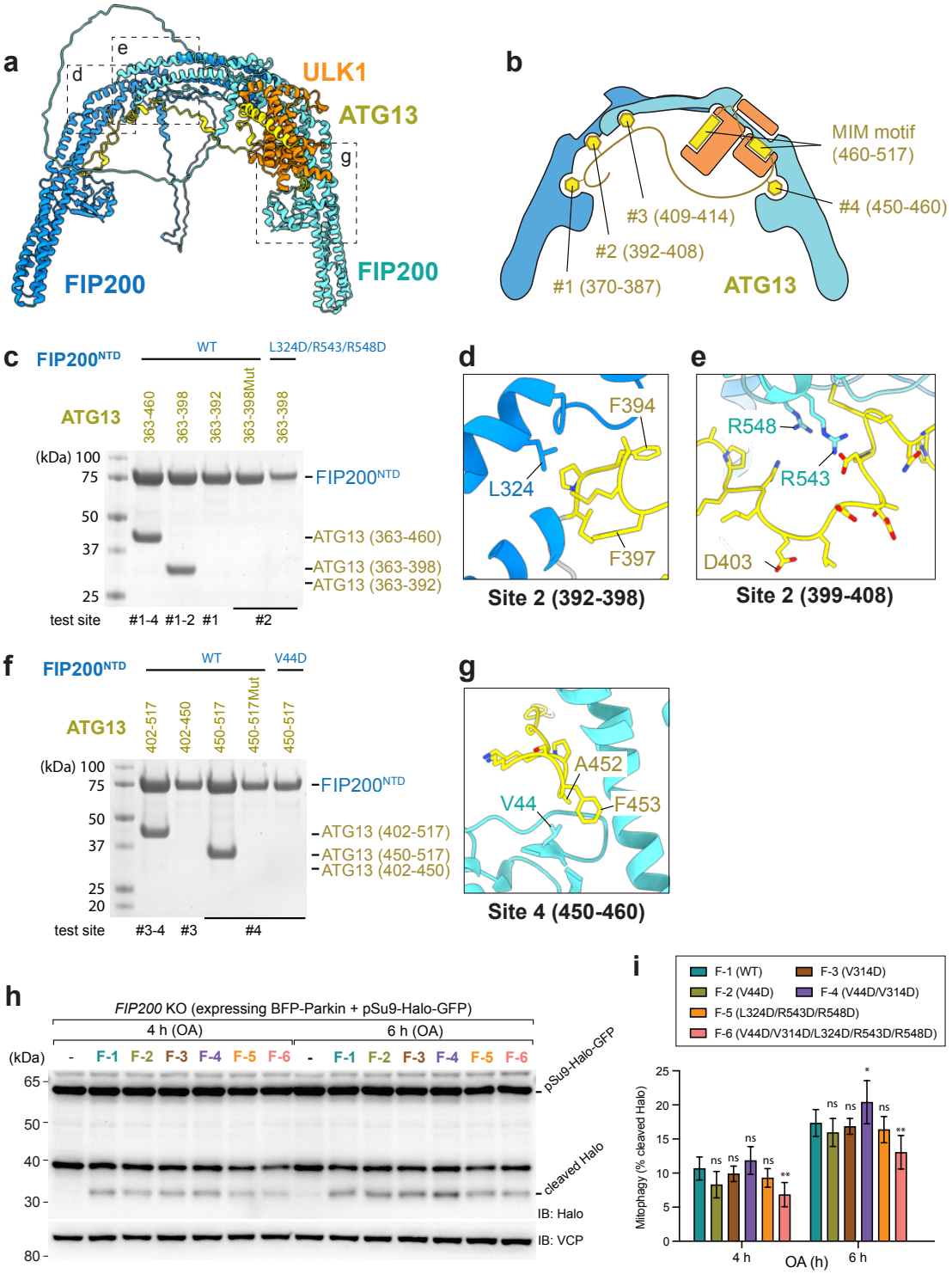
a
e
d
g
ULK1
ATG13
FIP200
FIP200
b
MIM motif
(460-517)
#4 (450-460)
#3 (409-414)
#2 (392-408)
#1 (370-387)
ATG13
c
FIP200NTD
WT
L324D/R543/R548D
ATG13
363-460
363-398
363-392
363-398Mut
363-398
(kDa) 100
75
50
37
25
FIP200NTD
ATG13 (363-460)
ATG13 (363-398)
ATG13 (363-392)
test site
#1-4 #1-2 #1
#2
d
F394
L324
F397
Site 2 (392-398)
e
R548
R543
D403
Site 2 (399-408)
f
FIP200NTD
WT
V44D
ATG13
402-517
402-450
450-517
450-517Mut
450-517
(kDa) 100
75
50
37
25
20
FIP200NTD
ATG13 (402-517)
ATG13 (450-517)
ATG13 (402-450)
test site
#3-4 #3
#4
g
A452
V44
F453
Site 4 (450-460)
h
FIP200 KO (expressing BFP-Parkin + pSu9-Halo-GFP)
4 h (OA)
6 h (OA)
(kDa)
-
F-1
F-2
F-3
F-4
F-5
F-6
65
50
40
30
80
pSu9-Halo-GFP
cleaved Halo
IB: Halo
IB: VCP
i
F-1 (WT)
F-2 (V44D)
F-3 (V314D)
F-4 (V44D/V314D)
F-5 (L324D/R543D/R548D)
F-6 (V44D/V314D/L324D/R543D/R548D)
Mitophagy (% cleaved Halo)
25
20
15
10
5
0
ns
**
*
4 h
OA (h)
6 h

Fig. 2 Investigation of the binding sites of ATG13^{IDR} on FIP200^{NTD}.

a. AlphaFold2 prediction model of the ULK1C core. **b**. Schematic diagram of the ULK1C core. **c-e,** Truncation and mutagenesis screening of the binding sites #2 and the corresponding key residues on the AlphaFold2 prediction model. 363-398Mut: ATG13$^{363-398}$ (F394D/F397D/E403K),. **f,g.** Truncation and mutagenesis screening of the binding sites #4 and the corresponding key residues on the AlphaFold2 prediction model. 450-517Mut: ATG13$^{450-517}$ (A452D). **h,i**. *FIP200* KO HeLa cells expressing BFP-Parkin and pSu9-Halo-GFP without rescue or rescued with different versions of mCherry-tagged FIP200 were treated with 50 nM TMR-conjugated Halo ligand for 15 min. Following that, cells were washed with 1xPBS and treated with OA for indicated time periods, harvested analyzed by immunoblotting with indicated antibodies (**h**) and the percentage of the cleaved Halo band was quantified (**i**). Data in (**i**) are mean mean ± s.d. from four independent experiments. ns: not significant, *P<0.05, **P<0.005 (two-way ANOVA).

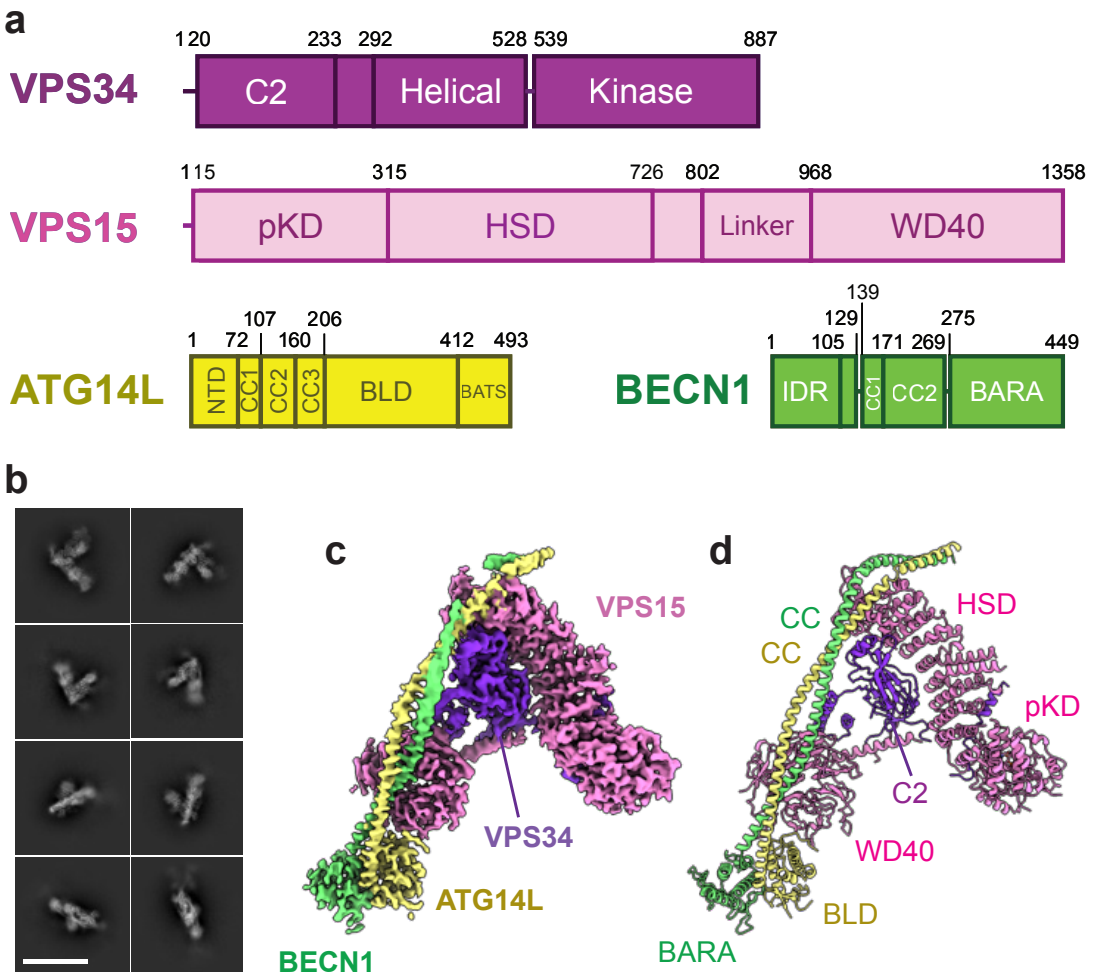

Fig. 3 Structure of PI3KC3-C1.

a. Domain organization of the PI3KC3-C1. pKD: pseudo-kinase domain, HSD: helical solenoid domain, NTD: N-terminal domain, CC: coiled-coil domain, BLD: BARA like domain, IDR: intrinsic disordered region. **b**. Representative 2D class averages of the PI3KC3-C1. Scale bar: 20 nm. **c**. Overview of the EM map and **d**. the coordinates of the PI3KC3-C1. The map is contoured at 7σ. Subunits are depicted in the following color code: VPS34: purple, VPS15: pink, BECN1: green, ATG14L: yellow. The main domains are indicated in the same color as in (**a**).

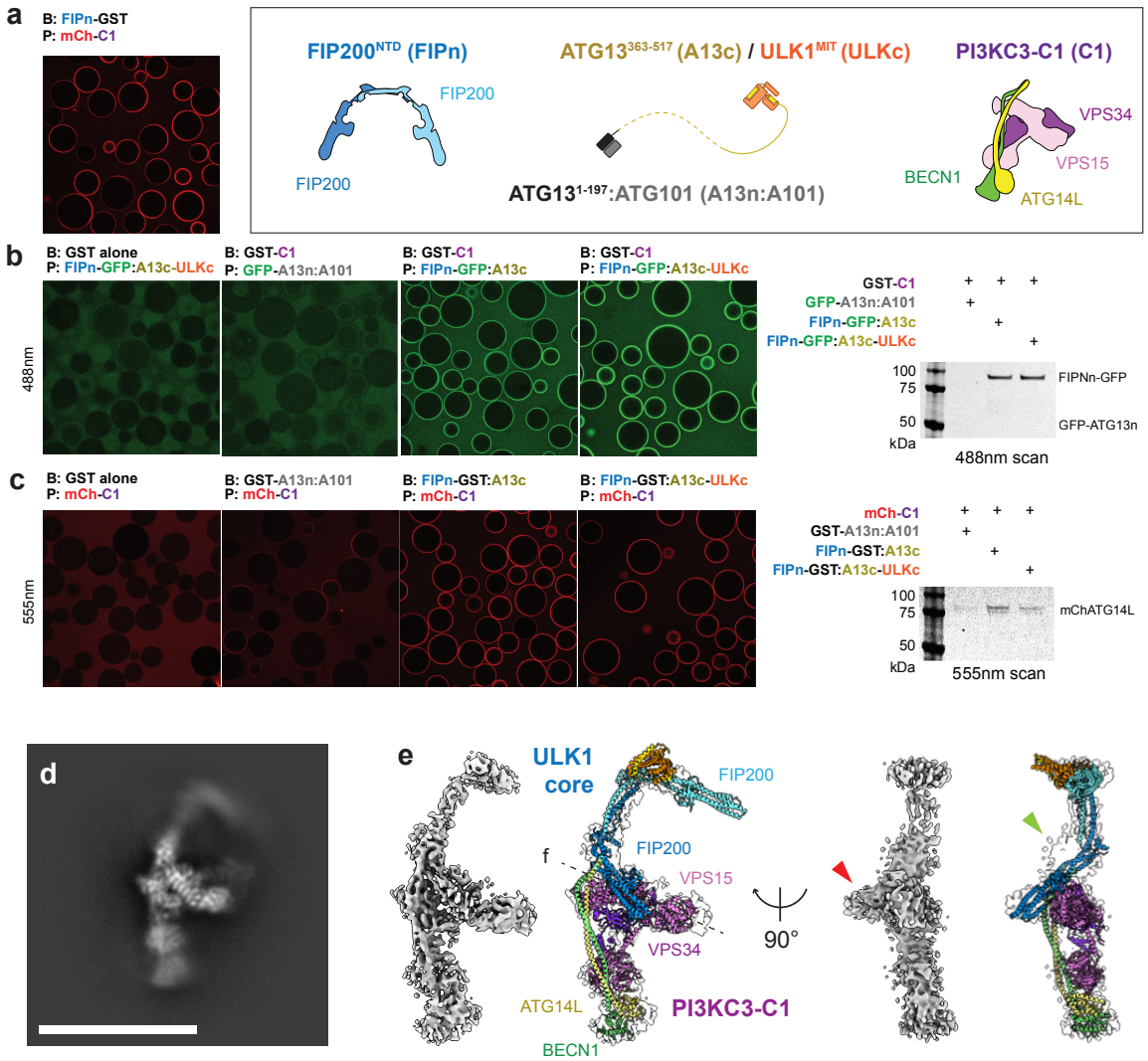

Fig. 4 Formation of the ULK1:PI3KC3-C1 supercomplex.

a. GSH beads coated with FIP200^{NTD} bound mCherry-PI3KC3-C1. The insert indicates each protein fragment and its abbreviation used in the following panels. **b**. GSH beads coated with GST-PI3KC3-C1 complex bound GFP-FIP200^{NTD} of ULK1C complex. **c**. GSH beads coated with GST-tagged FIP200^{NTD} core complex bound mCherry-PI3KC3-C1. **d**. Representative 2D class average of the ULK1:PI3KC3-C1 super complex. Scale bar: 20 nm. **e**. Overview of the rigid docking model of ULK1:PI3KC3-C1 super complex superposed with the EM map contoured at 7σ. Red arrow: EM density assigned to the FIP200^{Arm}. Green arrow: EM density assumed to be the BECN1^{NTD}-ATG14L^{NTD}.

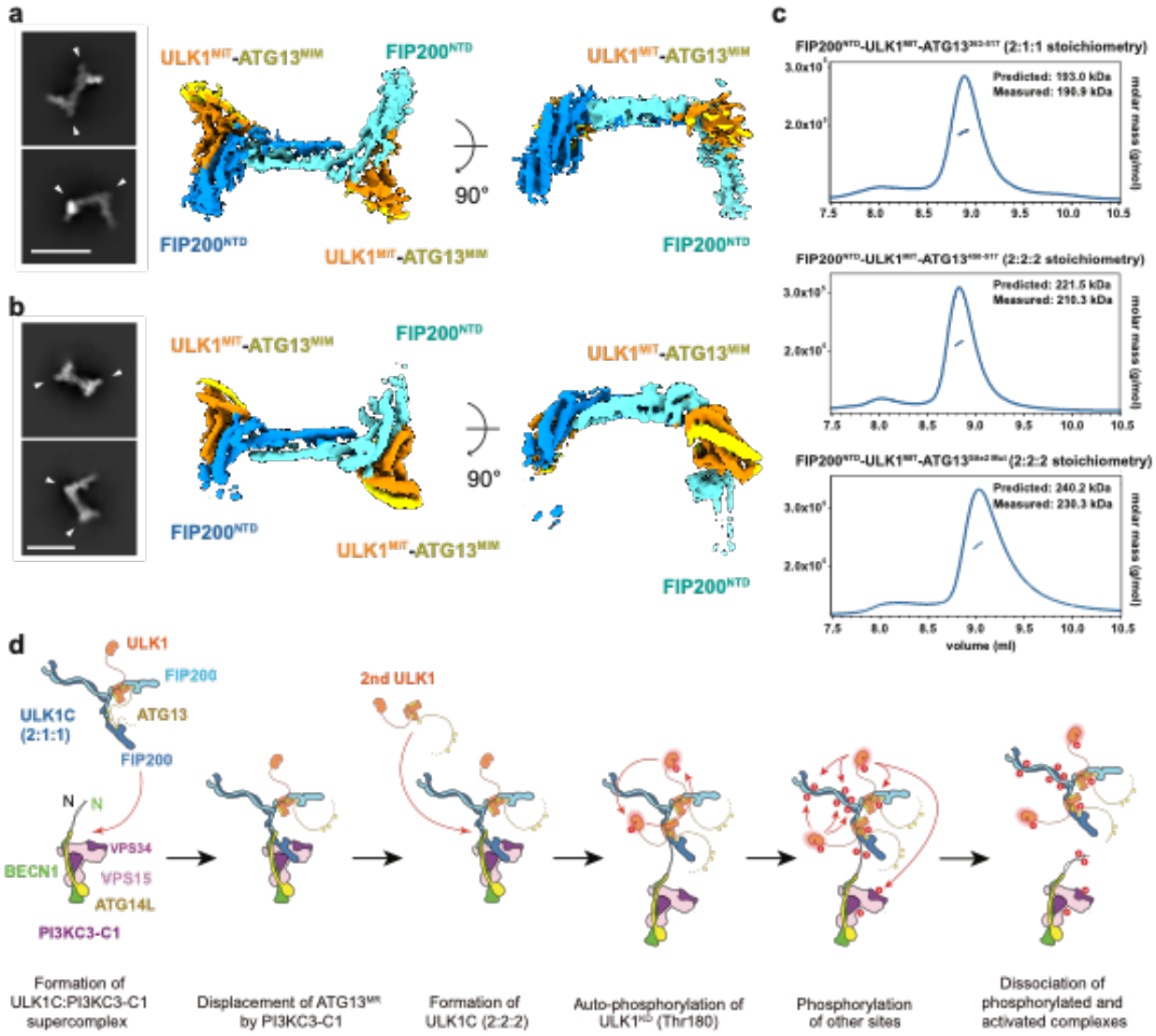
a
ULK1MIT-ATG13MIM
FIP200NTD
ULK1MIT-ATG13MIM
90°
FIP200NTD
ULK1MIT-ATG13MIM
FIP200NTD
b
ULK1MIT-ATG13MIM
FIP200NTD
ULK1MIT-ATG13MIM
90°
FIP200NTD
ULK1MIT-ATG13MIM
FIP200NTD
c
FIP200NTD-ULK1MIT-ATG13 (2:1:1 stoichiometry)
Predicted: 193.0 kDa
Measured: 198.9 kDa
FIP200NTD-ULK1MIT-ATG13 (2:2:2 stoichiometry)
Predicted: 221.5 kDa
Measured: 210.3 kDa
FIP200NTD-ULK1MIT-ATG13 (2:2:2 stoichiometry)
Predicted: 240.2 kDa
Measured: 230.3 kDa
molar mass (g/mol)
volume (ml)
d
ULK1
FIP200
ULK1C
(2:1:1)
ATG13
FIP200
N
N
VPS34
BECN1
VPS15
ATG14L
PI3KC3-C1
2nd ULK1
Formation of ULK1C:PI3KC3-C1 supercomplex
Displacement of ATG13MR by PI3KC3-C1
Formation of ULK1C (2:2:2)
Auto-phosphorylation of ULK1KD (Thr180)
Phosphorylation of other sites
Dissociation of phosphorylated and activated complexes

Fig. 5 Structures of the ULK1C (2:2:2) core and hypothesis for dimerization-dependent auto-activation of ULK1 kinase.

a. Representative 2D class average and the EM map of the ULK1C (2:2:2) core in the presence of PI3KC3-C1. The $ULK1^{MIT}$-$ATG13^{MIM}$ domain are indicated with white arrows. Scale bar: 20 nm. The EM map is contoured at 7σ. **b**. Representative 2D class average and the EM map of the ULK1C (2:2:2) core of the $ATG13^{450–517}$truncation mutant. The EM map is contoured at 14σ. **c**. SEC-MALS results of the ULK1C cores containing $ATG13^{363-517}$, $ATG13^{450-517}$, and $ATG13^{363-517}$ (F394D/F397D/E403K) mutant, respectively. The predicted and measured molecular weight of the complexes are shown. **d**. Hypothesis for the dimerization-dependent auto-phosphorylation and activation of ULK1 kinase.

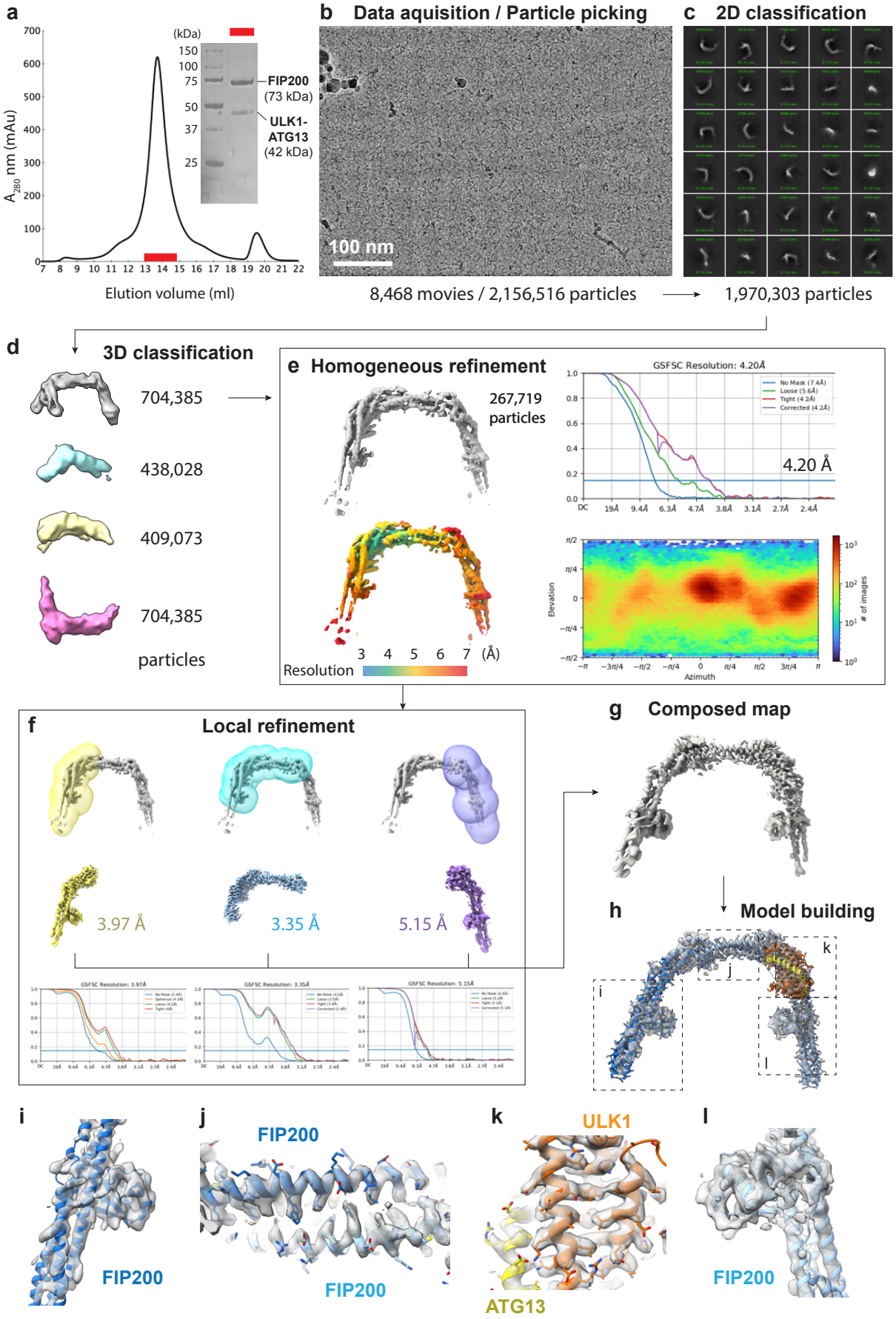
a
(kDa)
150
100
75
50
37
25
FIP200
(73 kDa)
ULK1-
ATG13
(42 kDa)
A_{280} nm (mAu)
Elution volume (ml)
b Data aquisition / Particle picking
100 nm
c 2D classification
8,468 movies / 2,156,516 particles
1,970,303 particles
d 3D classification
704,385
438,028
409,073
704,385
particles
e Homogeneous refinement
267,719
particles
GSFSC Resolution: 4.20Å
4.20 Å
Elevation
Azimuth
# of images
Resolution
3 4 5 6 7 (Å)
f Local refinement
3.97 Å
3.35 Å
5.15 Å
g Composed map
h Model building
i
j
k
l
FIP200
FIP200
FIP200
ULK1
ATG13
FIP200

Extended data Fig. 1 Cryo-EM sample preparation, image acquisition, data processing, and model building of ULK1C (2:1:1) core.

a. Size exclusion chromatography (SEC) profile of the ULK1C core. The inset shows an SDS-PAGE of the peak (red bar). **b**. A representative cryo-EM micrograph of the ULK1C core. **c**. Representative 2D class averages. **d**. Result of the first round of 3D classification. **e**. Global refinement of the final substack cleaned by multi-rounds of 3D classification. The FSC, local resolution, and angular distribution are shown accordingly. **f**. Masks for local refinement and the corresponding maps and FSCs. **g**. Final composed map for model building. **h**. Overview of the model building. The map is contoured at 12σ. **i-l**, Close-up views of the map superposed with the models. Each position is indicated in (**h**).

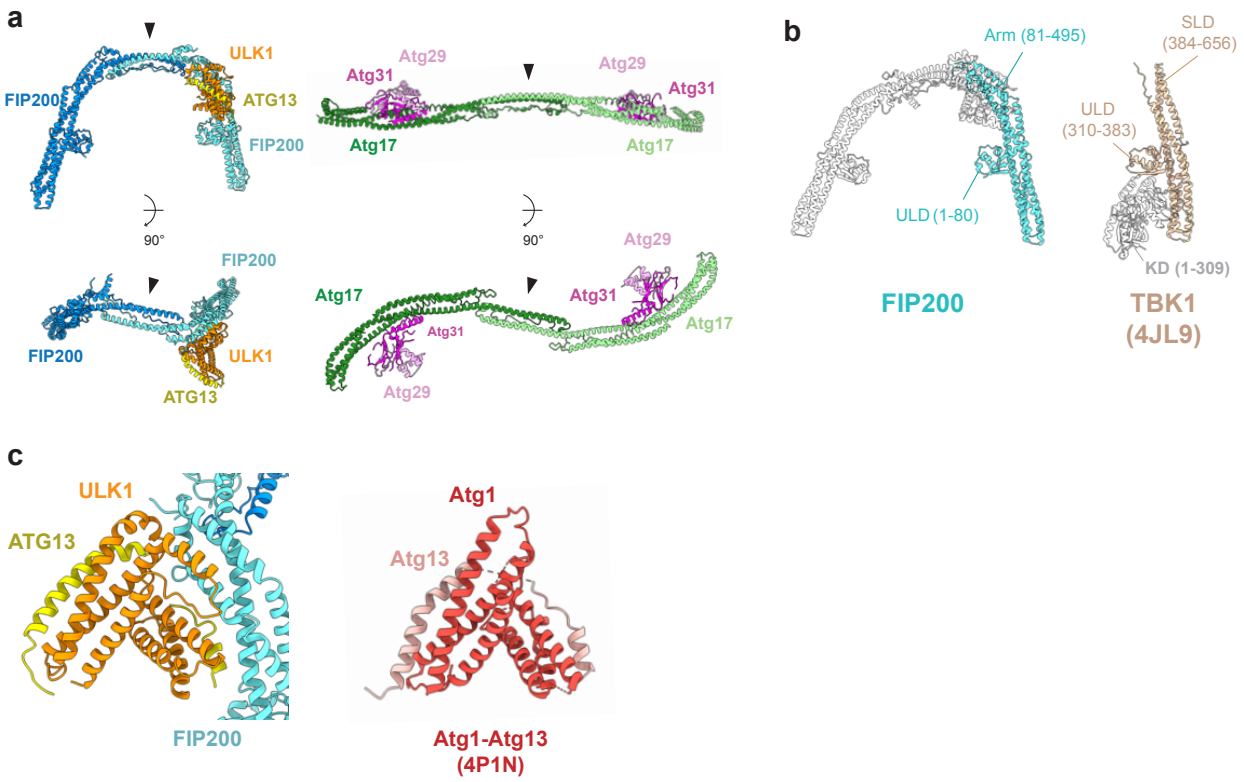

Extended data Fig. 2 Structural comparison of the ULK1C (2:1:1) core with related proteins.

a. Structural comparison of the FIP200 with its yeast homolog Atg17 (PDBID: 4HPQ). The dimerization domains are indicated with arrows. **b**. Structural comparison of the FIP200 with TBK1 (PDBID: 4JL9). **c.** Structural comparison of the ULK1-ATG13 heterodimer with its yeast homolog Atg1-Atg13 (PDBID: 4P1N).

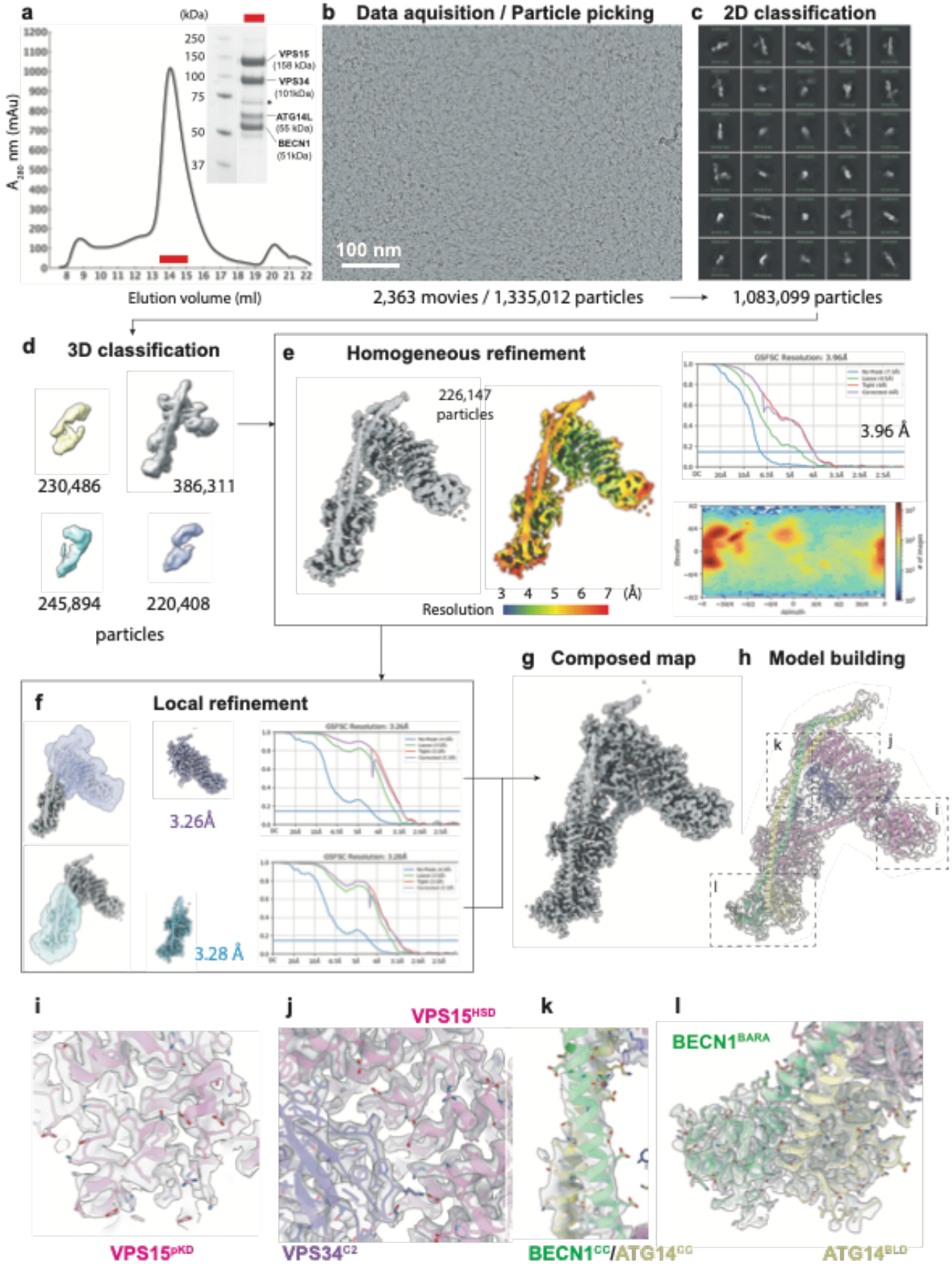
a
(kDa)
250
150
100
75
50
37
VPS15 (158 kDa)
VPS34 (101kDa)
ATG14L (55 kDa)
BECN1 (51kDa)
Elution volume (ml)
b Data aquisition / Particle picking
100 nm
c 2D classification
2,363 movies / 1,335,012 particles
1,083,099 particles
d 3D classification
230,486
386,311
245,894
220,408
particles
e Homogeneous refinement
226,147 particles
3.96 Å
Resolution
3 4 5 6 7 (Å)
f Local refinement
3.26Å
3.28 Å
g Composed map
h Model building
i
VPS15pKD
j
VPS15HSD
VPS34C2
k
BECN1CC/ATG14CC
l
BECN1BARA
ATG14BLD

Extended data Fig. 3 Cryo-EM sample preparation, image acquisition, data processing, and model building of PI3KC3-C1.

a. Size exclusion chromatography (SEC) profile of the PI3KC3-C1. The inset shows an SDS-PAGE of the peak (red bar). **b**. A representative cryo-EM micrograph of the PI3KC3-C1. **c**. Representative 2D class averages. **d**. Result of the first round of 3D classification. **e**. Global refinement of the final substack cleaned by multi-rounds of 3D classification. The FSC, local resolution, and angular distribution are shown accordingly. **f**. Masks for local refinement and the corresponding maps and FSCs. **g**. Final composed map for model building. **h**. Overview of the model building. The map is contoured at 7σ. **i-l**, Close-up views of the map superposed with the models. Each position is indicated in (**h**).

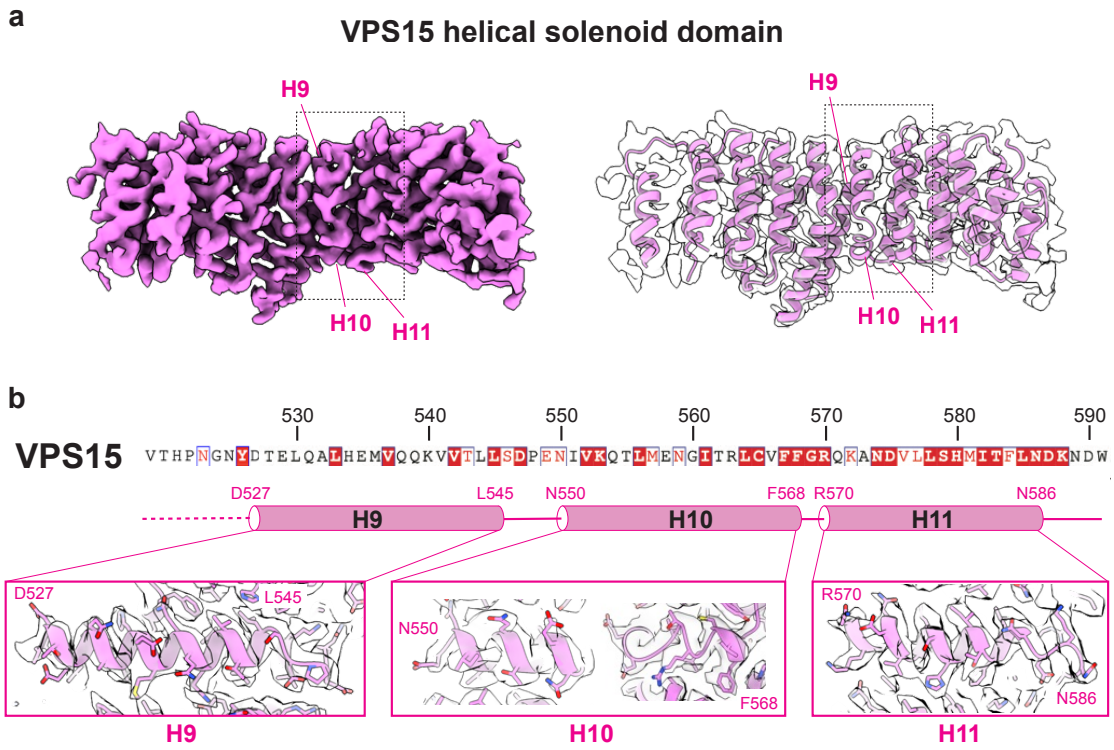

Extended data Fig. 4 Sequence assignment of the VPS15 helical solenoid domain.

a. EM map and the coordinates of the helical solenoid domain of VPS15. **b**. Sequence assignment and the close-up views of the 9-11th helixes of the helical solenoid domain. The map is contoured at 20σ.

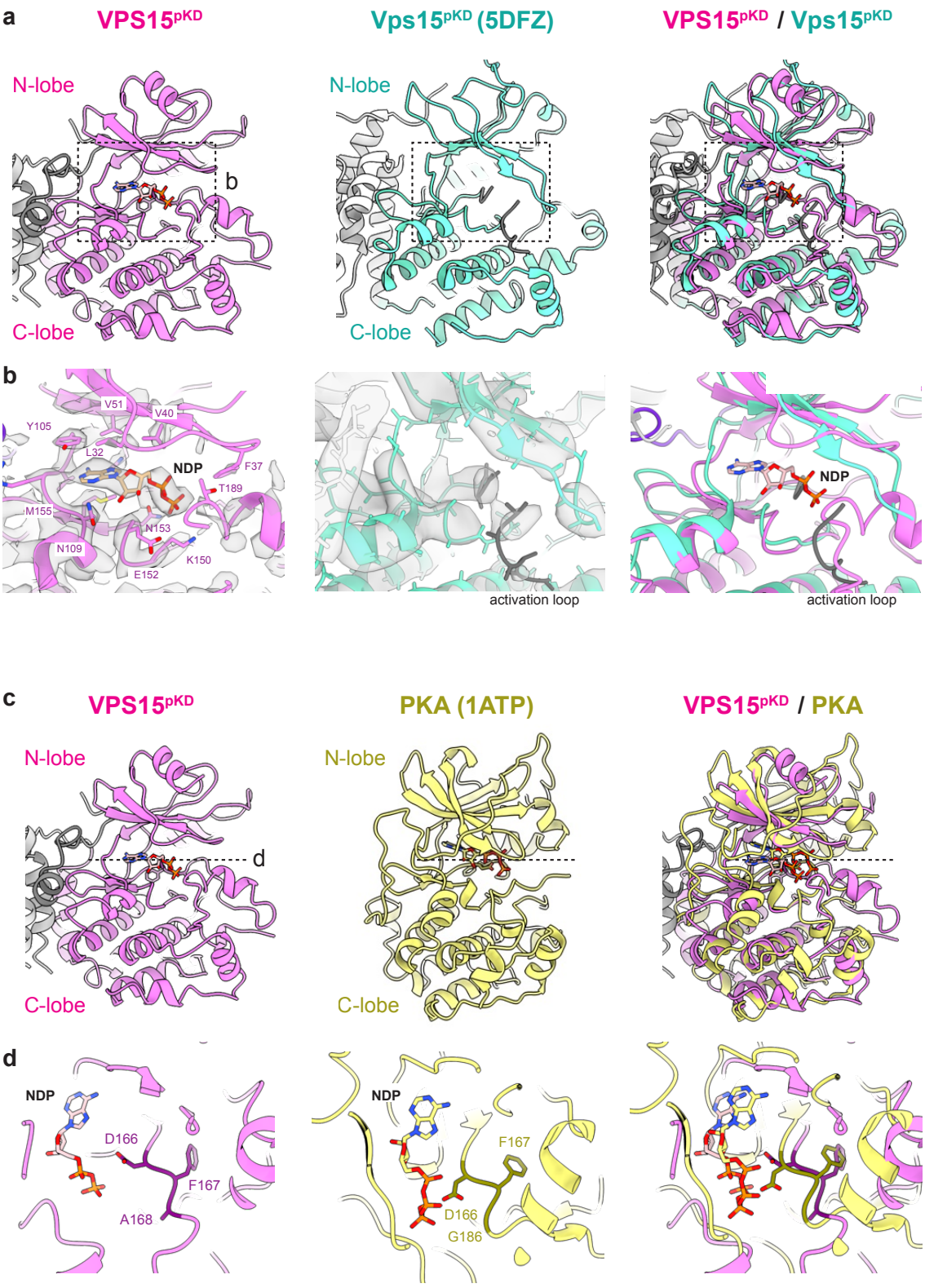
a
VPS15pKD
Vps15pKD (5DFZ)
VPS15pKD / Vps15pKD
N-lobe
C-lobe
b
b
V51
V40
Y105
L32
NDP
F37
T189
M155
N153
N109
K150
E152
activation loop
NDP
activation loop
c
VPS15pKD
PKA (1ATP)
VPS15pKD / PKA
N-lobe
C-lobe
d
d
NDP
D166
F167
A168
NDP
F167
D166
G186

Extended data Fig. 5 Structural comparison of the VPS15 pseudokinase domain with related proteins.

a. Comparison of the overall structure and **b**. the NDP binding pockets of the pseudokinase domain of human VPS15 and *S.cerevisiae* Vps15 (PDBID:5DFZ). The EM map of VPS15 and the electron density map of Vps15 are contoured at 20σ and 2σ, respectively. The dotted box indicates the zooming area in (**b**). **c**. Comparison of the overall structure and **d**. the NDP binding pockets of the pseudokinase domain of human VPS15 and kinase domain of Protein Kinase A (yellow) (PDBID:1ATP). The dotted line indicates the section plan shown in (**d**).

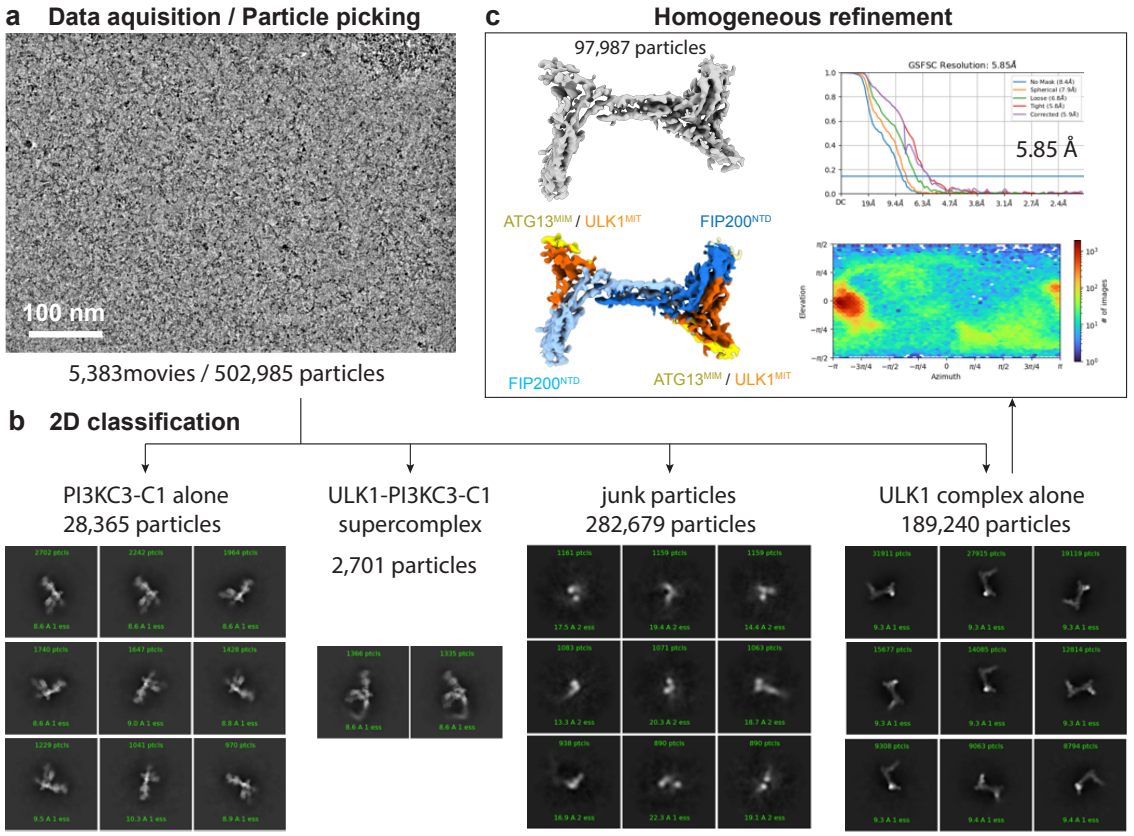
a Data aquisition / Particle picking
100 nm
5,383movies / 502,985 particles
c Homogeneous refinement
97,987 particles
GSFSC Resolution: 5.85Å
5.85 Å
ATG13MIM / ULK1MIT
FIP200NTD
FIP200NTD
ATG13MIM / ULK1MIT
b 2D classification
PI3KC3-C1 alone
28,365 particles
ULK1-PI3KC3-C1
supercomplex
2,701 particles
junk particles
282,679 particles
ULK1 complex alone
189,240 particles

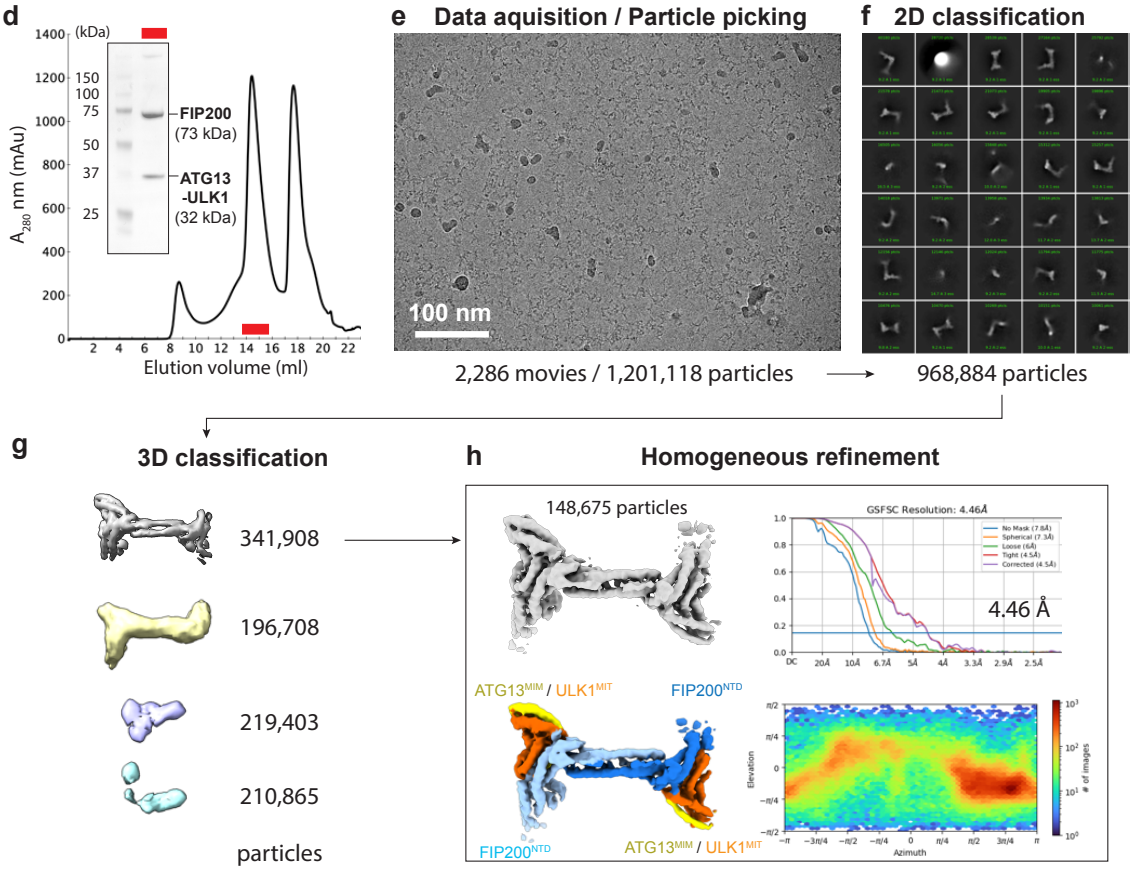
d
(kDa)
150
100
75
50
37
25
FIP200
(73 kDa)
ATG13
-ULK1
(32 kDa)
A280 nm (mAu)
Elution volume (ml)
e Data aquisition / Particle picking
100 nm
2,286 movies / 1,201,118 particles
f 2D classification
968,884 particles
g 3D classification
341,908
196,708
219,403
210,865
particles
h Homogeneous refinement
148,675 particles
GSFSC Resolution: 4.46Å
4.46 Å
ATG13MIM / ULK1MIT
FIP200NTD
FIP200NTD
ATG13MIM / ULK1MIT

Extended data Fig. 6 Structural determination of the the ULK1C (2:2:2) core in the PI3KC3-C1 mixture and the ATG13$^{450-517}$truncation mutant.

a. A representative cryo-EM micrograph of the ULK1C:PI3KC3-C1 mixture sample. **b**. Representative 2D class averages of four subpopulations of the dataset: 1) PI3KC3-C1 alone, 2) ULK1C:PI3KC3-C1 supercomplex, 3) junk particles, and 4) ULK1C alone. **c**. Result of the homogeneous refinement of the ULK1C alone substack. The FSC, local resolution, and angular distribution are shown accordingly. The EM map is contoured at 7σ. **d**. Size exclusion chromatography (SEC) profile of the ULK1C (2:2:2) core of ATG13$^{450-517}$ truncation mutant. The inset shows an SDS-PAGE of the peak (red bar). **e**. A representative cryo-EM micrograph of the ULK1C core containing the ATG13$^{450-517}$ truncation mutant. **f**. Representative 2D class averages. **g**. Result of the first round of 3D classification. **h**. Global refinement of the final substack. The FSC, local resolution, and angular distribution are shown accordingly.

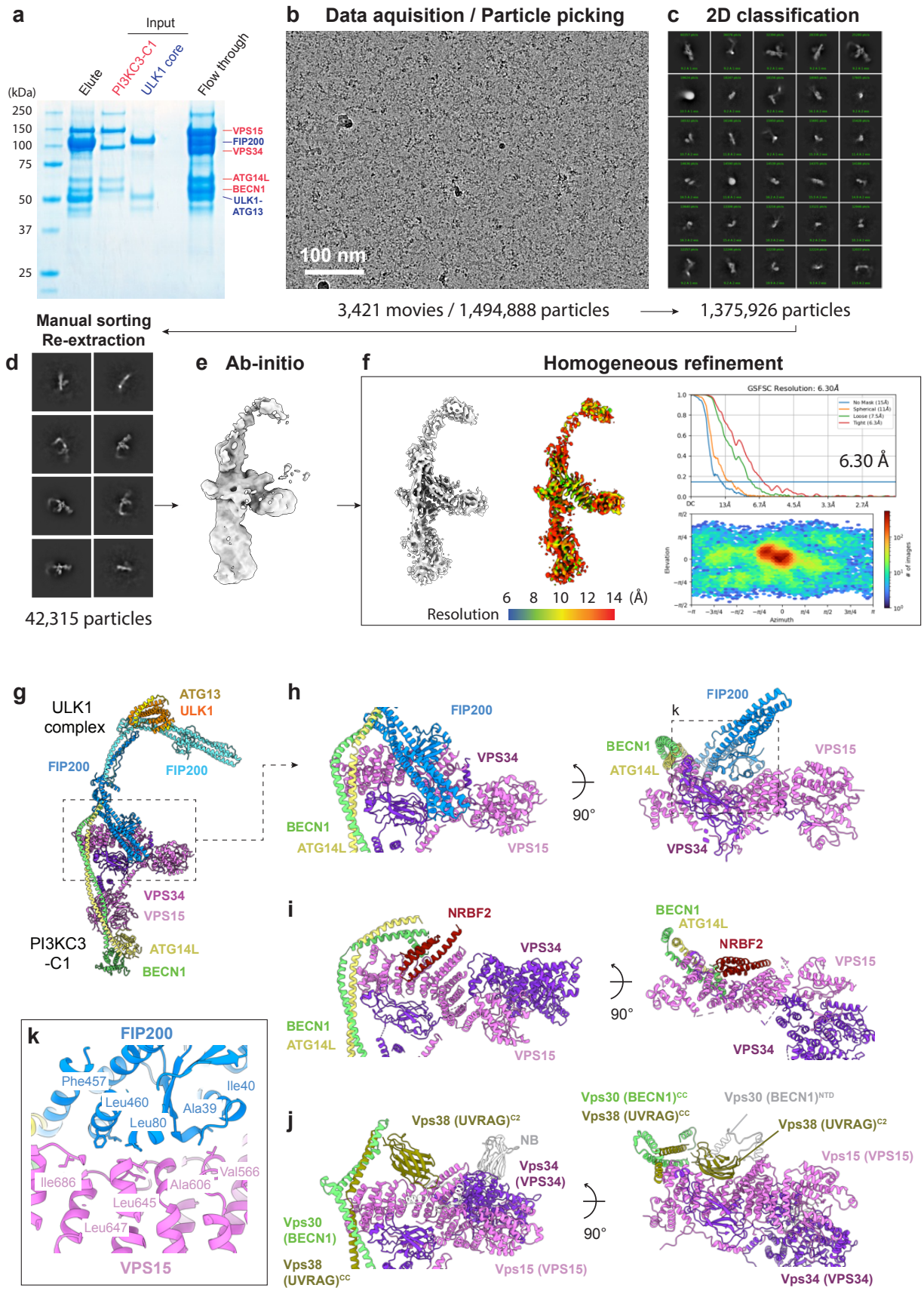
a
Input
Elute
PI3KC3-C1
ULK1 core
Flow through
(kDa)
250
150
100
75
50
37
25
VPS15
FIP200
VPS34
ATG14L
BECN1
ULK1-
ATG13
b Data aquisition / Particle picking
100 nm
c 2D classification
3,421 movies / 1,494,888 particles
1,375,926 particles
Manual sorting
Re-extraction
d
42,315 particles
e Ab-initio
f Homogeneous refinement
GSFSC Resolution: 6.30Å
6.30 Å
6 8 10 12 14 (Å)
Resolution
g
ULK1
complex
ATG13
ULK1
FIP200
FIP200
VPS34
VPS15
PI3KC3
-C1
ATG14L
BECN1
h
FIP200
VPS34
BECN1
ATG14L
VPS15
90°
FIP200
k
BECN1
ATG14L
VPS15
VPS34
i
NRBF2
VPS34
BECN1
ATG14L
VPS15
90°
BECN1
ATG14L
NRBF2
VPS15
VPS34
k
FIP200
Phe457
Ile40
Leu460
Ala39
Leu80
Ile686
Ala606
Val566
Leu645
Leu647
VPS15
j
Vps38 (UVRAG)C2
NB
Vps34
(VPS34)
Vps30
(BECN1)
Vps38
(UVRAG)CC
Vps15 (VPS15)
90°
Vps30 (BECN1)CC
Vps38 (UVRAG)CC
Vps30 (BECN1)NTD
Vps38 (UVRAG)C2
Vps15 (VPS15)
Vps34 (VPS34)

Extended data Fig. 7 Structural determination and comparison of the ULK1C:PI3KC3-C1 supercomplex.

a. SDS-PAGE of the ULK1C: PI3KC3-C1 pull-down sample. **b**. A representative cryo-EM micrograph. **c**. Representative 2D class averages. **d**. The 2D class averages of ULK1C: PI3KC3-C1 supercomplex are sorted by manual assessment. **e**. The initial model created from the substack (**d**). **f**. Result of the homogeneous refinement. The FSC, local resolution, and angular distribution are shown accordingly.

g. Overview of the ULK1C:PI3KC3-C1 supercomplex. **h-j**. Comparison of the VPS15/Vps15^{HSD} binding sites in binding with FIP200, NRBF2[18], and UVRAG[33], respectively. **k**. Close-up view of the interface between the FIP200^{NTD} and VPS15^{HSD}.

Reagent type (species) or resource	Designation	Source or reference	Identifiers	Additional information
Cell line (*Homo sapiens*)	HEK GnTi	ATCC	CRL-3022	
Recombinant DNA reagent	pCAG-FIP200 (1-640)	This paper		
Recombinant DNA reagent	pCAG-FIP200 (1-640)-MBP	This paper		
Recombinant DNA reagent	pCAG-FIP200 (1-640)-GST	This paper		
Recombinant DNA reagent	pCAG-FIP200 (1-640)-TSF	This paper		
Recombinant DNA reagent	pCAG-FIP200 (1-640)M2-TSF	This paper		
Recombinant DNA reagent	pCAG-FIP200 (1-640)M3-TSF	This paper		
Recombinant DNA reagent	pCAG-FIP200 (1-640)-msfGFP	This paper		
Recombinant DNA reagent	pCAG-TSF-ATG13 (363-517)-ULK1 (836-1050)	This paper		
Recombinant DNA reagent	pCAG-TSF-ATG13 (450-517)-ULK1 (836-1050)	This paper		
Recombinant DNA reagent	pCAG-ATG13 (363-517)-ULK1 (836-1050)-TSF	This paper		
Recombinant DNA reagent	pCAG-TSF-ATG13 (363-517)	This paper		
Recombinant DNA reagent	pCAG-GST-ATG13 (363-517)	This paper		
Recombinant DNA reagent	pCAG-GST-ATG13 (460-517)	This paper		
Recombinant DNA reagent	pCAG-GST-ATG13 (363-460)	This paper		
Recombinant DNA reagent	pCAG-GST-ATG13 (363-398)	This paper		
Recombinant DNA reagent	pCAG-GST-ATG13 (363-398)Mut	This paper		
Recombinant DNA reagent	pCAG-GST-ATG13 (363-392)	This paper		
Recombinant DNA reagent	pCAG-GST-ATG13 (402-517)	This paper		
Recombinant DNA reagent	pCAG-GST-ATG13 (402-450)	This paper		

Recombinant DNA reagent	pCAG-GST-ATG13 (450-517)	This paper		
Recombinant DNA reagent	pCAG-GST-ATG13 (450-517)Mut	This paper		
Recombinant DNA reagent	pCAG-GST-ATG13 (1-197)	This paper		
Recombinant DNA reagent	pCAG-msfGFP-ATG13 (1-197)	This paper		
Recombinant DNA reagent	pCAG-TSF-ATG101	https://doi.org/10.1083/jcb.201911047		
Recombinant DNA reagent	pCAG-ATG101	https://doi.org/10.1083/jcb.201911047		
Recombinant DNA reagent	pCAG-ATG13 (363-517)-MBP	This paper		
Recombinant DNA reagent	pCAG-ULK1 (836-1050)-MBP	This paper		
Recombinant DNA reagent	pCAG-VPS15-TSF	This paper		
Recombinant DNA reagent	pCAG-VPS34	This paper		
Recombinant DNA reagent	pCAG-ATG14	This paper		
Recombinant DNA reagent	pCAG-GST-ATG14	This paper		
Recombinant DNA reagent	pCAG-mCherry-ATG14	This paper		
Recombinant DNA reagent	pCAG-BECN1	This paper		
Software, algorithm				
Software, algorithm	coot	https://www2.mrc-lmb.cam.ac.uk/personal/pemsley/coot/		
Software, algorithm	pymol	https://pymol.org/2/		
	Chimera	https://www.cgl.ucsf.edu/chimera/		
Other	Glutathione Sepharose 4B GST-tagged protein purification resin	GE healthcare, Chicago, IL	Cat#17075605	
Other	Amylose Resin	New England Biolabs, Ipswich, MA	Cat#E8021L	
Other	Strep-Tactin Superflow high capacity 50% suspension	IBA Lifesciences, Göttingen, Germany	Cat# 2-1208-010	

Extended Data Table 1. List of expression constructs used in this study.

	ULK1C core (2:1:1) stoichiometry	PI3KC3-C1	ULK1C:PI3KC3-C1 supercomplex	ULK1C core (2:2:2) stoichiometry in PI3KC3-C1 mixture	ULK1C core (2:2:2) stoichiometry ATG13$^{450-517}$ mutant
	EMD-40658 8SOI	EMD-40669 8SOR	EMD-40738 8SRQ	EMD-40715 8SQZ	EMD-40735 8SRM
Data collection and processing					
Magnification	81,000	36,000	36,000	81,000	36,000
Voltage (kV)	300	200	200	300	200
Electron exposure ($e^-/Å^2$)	50	50	50	50	50
Defocus range (μm)	-0.8 to -2.0	-0.8 to -2.0	-0.8 to -2.0	-0.8 to -2.0	-0.8 to -2.0
Physical pixel size (Å)	1.05	1.115	1.115	1.05	1.115
Symmetry imposed	C1	C1	C1	C1	C1
Images	8,468	2,243	3,421	5,383	2,286
Initial particle images (no.)	2,156,516	1,229,932	1,375,926	502,985	968,884
Final particle images (no.)	267,719	226,147	42,315	97,987	149,409
Map resolution, Global (Å)	4.2	3.93	6.3	5.28	4.46
Map resolution, Best local (Å)	3.35	3.26	n/a	n/a	n/a
FSC threshold	0.143	0.143	0.143	0.143	0.143
Refinement					
Map sharpening B factor (A^2)	143.2	100.6	560.9	431.6	155.4
Model composition					
Non-hydrogen atoms	10243	16048	16051	7438	5773
Protein residues	1276	1986	3237	1498	1163
Ligands	0	1	0	0	0
B factors ($Å^2$)					
Protein	126.43	55.99	421.54	319.79	208.69
Ligands	n/a	33.75	n/a	n/a	n/a
R.m.s. deviations					
Bond lengths (Å)	0.003	0.003	0.003	0.004	0.002
Bond angles (°)	0.598	0.551	0.659	0.633	0.405
Validation					
MolProbity score	1.7	1.75	1.35	1.95	1.51
Clashscore	9.52	7.36	2.94	8.07	4.44
Poor rotamers (%)	1.5	1.5	n/a	n/a	n/a
Ramachandran plot					
Favored (%)	96.75	95.32	96.05	91.41	95.87
Allowed (%)	3.17	4.63	3.88	8.59	4.13
Disallowed(%)	0.008	0.05	0.06	0	0

Extended Data Table 2. Cryo-EM sample preparation, data collection and refinement statistics.

References

1 Yamamoto, H., Zhang, S. & Mizushima, N. Autophagy genes in biology and disease. *Nat Rev Genet*, 1-19 (2023). https://doi.org:10.1038/s41576-022-00562-w

2 Menzies, F. M. *et al.* Autophagy and Neurodegeneration: Pathogenic Mechanisms and Therapeutic Opportunities. *Neuron* **93**, 1015-1034 (2017). https://doi.org:10.1016/j.neuron.2017.01.022

3 Themistokleous, C., Bagnoli, E., Parulekar, R. & Muqit, M. M. K. Role of autophagy pathway in Parkinson's disease and related Genetic Neurological disorders. *J Mol Biol*, 168144 (2023). https://doi.org:10.1016/j.jmb.2023.168144

4 Hara, T. *et al.* FIP200, a ULK-interacting protein, is required for autophagosome formation in mammalian cells. *J Cell Biol* **181**, 497-510 (2008). https://doi.org:10.1083/jcb.200712064

5 Itakura, E. & Mizushima, N. Characterization of autophagosome formation site by a hierarchical analysis of mammalian Atg proteins. *Autophagy* **6**, 764-776 (2010). https://doi.org:10.4161/auto.6.6.12709

6 Karanasios, E. *et al.* Dynamic association of the ULK1 complex with omegasomes during autophagy induction. *J Cell Sci* **126**, 5224-5238 (2013). https://doi.org:10.1242/jcs.132415

7 Itakura, E., Kishi, C., Inoue, K. & Mizushima, N. Beclin 1 forms two distinct phosphatidylinositol 3-kinase complexes with mammalian Atg14 and UVRAG. *Molecular Biology of the Cell* **19**, 5360-5372 (2008).

8 Hamasaki, M. *et al.* Autophagosomes form at ER-mitochondria contact sites. *Nature* **495**, 389-393 (2013). https://doi.org:10.1038/nature11910

9 Ge, L., Melville, D., Zhang, M. & Schekman, R. The ER-Golgi intermediate compartment is a key membrane source for the LC3 lipidation step of autophagosome biogenesis. *Elife* **2**, e00947 (2013). https://doi.org:10.7554/eLife.00947

10 Hosokawa, N. *et al.* Nutrient-dependent mTORC1 Association with the ULK1-Atg13-FIP200 Complex Required for Autophagy. *Molecular Biology of the Cell* **20**, 1981-1991 (2009).

11 Ganley, I. G., Lam, D. H., Wang, J., Ding, X., Chen, S. & Jiang, X. ULK1-ATG13-FIP200 complex mediates mTOR signaling and is essential for autophagy. *Journal of Biological Chemistry* **284**, 12297-12305 (2009).

12 Jung, C. H. *et al.* ULK-Atg13-FIP200 Complexes Mediate mTOR Signaling to the Autophagy Machinery. *Molecular Biology of the Cell* **20**, 1992-2003 (2009).

13 Mercer, C. A., Kaliappan, A. & Dennis, P. B. A novel, human Atg13 binding protein, Atg101, interacts with ULK1 and is essential for macroautophagy. *Autophagy.* **5** (2009).

14 Hosokawa, H., Sasaki, T., Iemura, S., Natsume, T., Hara, T. & Mizushima, N. Atg101, a novel mammalian autophagy protein interacting with Atg13. *Autophagy* **5**, 973-979 (2009).

15 Ohashi, Y., Tremel, S. & Williams, R. L. VPS34 complexes from a structural perspective. *J Lipid Res* **60**, 229-241 (2019). https://doi.org:10.1194/jlr.R089490

16 Lin, M. G. & Hurley, J. H. Structure and function of the ULK1 complex in autophagy. *Curr Opin Cell Biol* **39**, 61-68 (2016). https://doi.org:10.1016/j.ceb.2016.02.010

17 Matoba, K. & Noda, N. N. Structural catalog of core Atg proteins opens new era of autophagy research. *J Biochem* **169**, 517-525 (2021). https://doi.org:10.1093/jb/mvab017

18 Young, L. N., Goerdeler, F. & Hurley, J. H. Structural pathway for allosteric activation of the autophagic PI 3-kinase complex I. *Proc Natl Acad Sci U S A* **116**, 21508-21513 (2019). https://doi.org:10.1073/pnas.1911612116

19 Tremel, S. *et al.* Structural basis for VPS34 kinase activation by Rab1 and Rab5 on membranes. *Nat Commun* **12**, 1564 (2021). https://doi.org:10.1038/s41467-021-21695-2

20 Shi, X., Yokom, A. L., Wang, C., Young, L. N., Youle, R. J. & Hurley, J. H. ULK complex organization in autophagy by a C-shaped FIP200 N-terminal domain dimer. *J Cell Biol* **219** (2020). https://doi.org:10.1083/jcb.201911047
21 Galluzzi, L., Bravo-San Pedro, J. M., Levine, B., Green, D. R. & Kroemer, G. Pharmacological modulation of autophagy: therapeutic potential and persisting obstacles. *Nat Rev Drug Discov* **16**, 487-511 (2017). https://doi.org:10.1038/nrd.2017.22
22 Russell, R. C. *et al.* ULK1 induces autophagy by phosphorylating Beclin-1 and activating VPS34 lipid kinase. *Nature Cell Biology* **15**, 741-750 (2013). https://doi.org:10.1038/ncb2757
23 Egan, D. F. *et al.* Small Molecule Inhibition of the Autophagy Kinase ULK1 and Identification of ULK1 Substrates. *Mol Cell* **59**, 285-297 (2015). https://doi.org:10.1016/j.molcel.2015.05.031
24 Park, J. M. *et al.* The ULK1 complex mediates MTORC1 signaling to the autophagy initiation machinery via binding and phosphorylating ATG14. *Autophagy* **12**, 547-564 (2016). https://doi.org:10.1080/15548627.2016.1140293
25 Mercer, T. J. *et al.* Phosphoproteomic identification of ULK substrates reveals VPS15-dependent ULK/VPS34 interplay in the regulation of autophagy. *Embo j* **40**, e105985 (2021). https://doi.org:10.15252/embj.2020105985
26 Fujioka, Y. *et al.* Structural basis of starvation-induced assembly of the autophagy initiation complex. *Nat Struct Mol Biol* **21**, 513-521 (2014). https://doi.org:10.1038/nsmb.2822
27 Ragusa, M. J., Stanley, R. E. & Hurley, J. H. Architecture of the Atg17 complex as a scaffold for autophagosome biogenesis. *Cell* **151**, 1501-1512 (2012). https://doi.org:10.1016/j.cell.2012.11.028
28 Nguyen, T. N. *et al.* Unconventional initiation of PINK1/Parkin mitophagy by Optineurin. *Mol Cell* **83**, 1693-1709.e1699 (2023). https://doi.org:10.1016/j.molcel.2023.04.021
29 Chan, E. Y., Longatti, A., McKnight, N. C. & Tooze, S. A. Kinase-inactivated ULK proteins inhibit autophagy via their conserved C-terminal domains using an Atg13-independent mechanism. *Mol Cell Biol* **29**, 157-171 (2009). https://doi.org:10.1128/MCB.01082-08
30 Jumper, J. *et al.* Highly accurate protein structure prediction with AlphaFold. *Nature* **596**, 583-589 (2021). https://doi.org:10.1038/s41586-021-03819-2
31 Nguyen, T. N. *et al.* Unconventional initiation of PINK1/Parkin mitophagy by Optineurin. *Molecular cell* **83**, 1693-1709 (2023). https://doi.org:10.1016/j.molcel.2023.04.021
32 Baskaran, S. *et al.* Architecture and dynamics of the autophagic phosphatidylinositol 3-kinase complex. *Elife* **3** (2014). https://doi.org:10.7554/eLife.05115
33 Rostislavleva, K. *et al.* Structure and flexibility of the endosomal Vps34 complex reveals the basis of its function on membranes. *Science* **350**, aac7365 (2015). https://doi.org:10.1126/science.aac7365
34 Ma, M. *et al.* Cryo-EM structure and biochemical analysis reveal the basis of the functional difference between human PI3KC3-C1 and -C2. *Cell Res* **27**, 989-1001 (2017). https://doi.org:10.1038/cr.2017.94
35 Stjepanovic, G., Baskaran, S., Lin, M. G. & Hurley, J. H. Vps34 Kinase Domain Dynamics Regulate the Autophagic PI 3-Kinase Complex. *Mol Cell* **67**, 528-534 e523 (2017). https://doi.org:10.1016/j.molcel.2017.07.003
36 Chang, C. *et al.* Bidirectional Control of Autophagy by BECN1 BARA Domain Dynamics. *Mol Cell* **73**, 339-353 e336 (2019). https://doi.org:10.1016/j.molcel.2018.10.035
37 Cook, A. S. I. *et al.* Structural pathway for class III PI 3-kinase activation by the myristoylated GTP-binding pseudokinase VPS15. *bioRxiv* (2023).
38 Hurley, J. H. & Young, L. N. Mechanisms of Autophagy Initiation. *Annu Rev Biochem* **86**, 225-244 (2017). https://doi.org:10.1146/annurev-biochem-061516-044820
39 Maday, S. & Holzbaur, E. L. Compartment-Specific Regulation of Autophagy in Primary Neurons. *J Neurosci* **36**, 5933-5945 (2016). https://doi.org:10.1523/jneurosci.4401-15.2016

40 Nguyen, A. *et al.* Metamorphic proteins at the basis of human autophagy initiation and lipid transfer. *Mol Cell* (2023). https://doi.org:10.1016/j.molcel.2023.04.026
41 Hitomi, K., Kotani, T., Noda, N. N., Kimura, Y. & Nakatogawa, H. The Atg1 complex, Atg9, and Vac8 recruit PI3K complex I to the pre-autophagosomal structure. *J Cell Biol* **222** (2023). https://doi.org:10.1083/jcb.202210017
42 Lazarus, M. B., Novotny, C. J. & Shokat, K. M. Structure of the Human Autophagy Initiating Kinase ULK1 in Complex with Potent Inhibitors. *Acs Chemical Biology* **10**, 257-261 (2015). https://doi.org:10.1021/cb500835z
43 Yeh, Y. Y., Wrasman, K. & Herman, P. K. Autophosphorylation within the Atg1 activation loop is required for both kinase activity and the induction of autophagy in Saccharomyces cerevisiae. *Genetics* **185**, 871-882 (2010). https://doi.org:10.1534/genetics.110.116566
44 Yeh, Y. Y., Shah, K. H. & Herman, P. K. An Atg13 protein-mediated self-association of the Atg1 protein kinase is important for the induction of autophagy. *J Biol Chem* **286**, 28931-28939 (2011). https://doi.org:10.1074/jbc.M111.250324
45 Torggler, R. *et al.* Two Independent Pathways within Selective Autophagy Converge to Activate Atg1 Kinase at the Vacuole. *Mol Cell* **64**, 221-235 (2016). https://doi.org:10.1016/j.molcel.2016.09.008
46 Lemmon, M. A. & Schlessinger, J. Cell signaling by receptor tyrosine kinases. *Cell* **141**, 1117-1134 (2010). https://doi.org:10.1016/j.cell.2010.06.011
47 Herman, P. K., Stack, J. H., DeModena, J. A. & Emr, S. D. A novel protein kinase homolog essential for protein sorting to the yeast lysosome-like vacuole. *Cell* **64**, 425-437 (1991). https://doi.org:10.1016/0092-8674(91)90650-n
48 Egan, D. F. *et al.* Phosphorylation of ULK1 (hATG1) by AMP-activated protein kinase connects energy sensing to mitophagy. *Science* **331**, 456-461 (2011). https://doi.org:10.1126/science.1196371
49 Thurston, T. L., Ryzhakov, G., Bloor, S., von Muhlinen, N. & Randow, F. The TBK1 adaptor and autophagy receptor NDP52 restricts the proliferation of ubiquitin-coated bacteria. *Nat Immunol* **10**, 1215-1221 (2009). https://doi.org:10.1038/ni.1800
50 Adriaenssens, E., Ferrari, L. & Martens, S. Orchestration of selective autophagy by cargo receptors. *Curr Biol* **32**, R1357-r1371 (2022). https://doi.org:10.1016/j.cub.2022.11.002
51 Zheng, Q. *et al.* Calcium transients on the ER surface trigger liquid-liquid phase separation of FIP200 to specify autophagosome initiation sites. *Cell* **185**, 4082-4098.e4022 (2022). https://doi.org:10.1016/j.cell.2022.09.001
52 Lazarou, M. *et al.* The ubiquitin kinase PINK1 recruits autophagy receptors to induce mitophagy. *Nature* **524**, 309-314 (2015). https://doi.org:10.1038/nature14893
53 Yim, W. W., Yamamoto, H. & Mizushima, N. A pulse-chasable reporter processing assay for mammalian autophagic flux with HaloTag. *Elife* **11** (2022). https://doi.org:10.7554/eLife.78923
54 Nguyen, T. N. *et al.* ATG4 family proteins drive phagophore growth independently of the LC3/GABARAP lipidation system. *Molecular cell* **81**, 2013-2030 e2019 (2021). https://doi.org:10.1016/j.molcel.2021.03.001
55 Ahn, E. *et al.* Batch Production of High-Quality Graphene Grids for Cryo-EM: Cryo-EM Structure of Methylococcus capsulatus Soluble Methane Monooxygenase Hydroxylase. *ACS Nano* **17**, 6011-6022 (2023). https://doi.org:10.1021/acsnano.3c00463
56 Mastronarde, D. N. Automated electron microscope tomography using robust prediction of specimen movements. *J Struct Biol* **152**, 36-51 (2005). https://doi.org:10.1016/j.jsb.2005.07.007
57 Punjani, A., Rubinstein, J. L., Fleet, D. J. & Brubaker, M. A. cryoSPARC: algorithms for rapid unsupervised cryo-EM structure determination. *Nat Methods* **14**, 290-296 (2017). https://doi.org:10.1038/nmeth.4169

58 Bepler, T. *et al.* Positive-unlabeled convolutional neural networks for particle picking in cryo-electron micrographs. *Nat Methods* **16**, 1153-1160 (2019). https://doi.org:10.1038/s41592-019-0575-8
59 Pettersen, E. F. *et al.* UCSF ChimeraX: Structure visualization for researchers, educators, and developers. *Protein Sci* **30**, 70-82 (2021). https://doi.org:10.1002/pro.3943
60 Tang, G. *et al.* EMAN2: an extensible image processing suite for electron microscopy. *J Struct Biol* **157**, 38-46 (2007). https://doi.org:10.1016/j.jsb.2006.05.009
61 Croll, T. I. ISOLDE: a physically realistic environment for model building into low-resolution electron-density maps. *Acta Crystallogr D Struct Biol* **74**, 519-530 (2018). https://doi.org:10.1107/S2059798318002425
62 Emsley, P. & Cowtan, K. Coot: model-building tools for molecular graphics. *Acta Crystallogr D Biol Crystallogr* **60**, 2126-2132 (2004). https://doi.org:10.1107/S0907444904019158
63 Liebschner, D. *et al.* Macromolecular structure determination using X-rays, neutrons and electrons: recent developments in Phenix. *Acta Crystallogr D Struct Biol* **75**, 861-877 (2019). https://doi.org:10.1107/S2059798319011471
64 Berman, H., Henrick, K. & Nakamura, H. Announcing the worldwide Protein Data Bank. *Nat Struct Biol* **10**, 980 (2003). https://doi.org:10.1038/nsb1203-980
65 Westbrook, J., Feng, Z., Burkhardt, K. & Berman, H. M. Validation of protein structures for protein data bank. *Methods Enzymol* **374**, 370-385 (2003). https://doi.org:10.1016/S0076-6879(03)74017-8